UNIVERSITI TEKNIKAL MALAYSIA MELAKA

HEAT TRANSPORT AND ADSORPTION MECHANISM OF LINEAR ALKANE LIQUIDS ON SOLID SURFACES

RANJINI DEVI A/P RAMA

MASTER OF SCIENCE IN MECHANICAL ENGINEERING

2025

Faculty of Mechanical Technology and Engineering

HEAT TRANSPORT AND ADSORPTION MECHANISM OF LINEAR ALKANE LIQUIDS ON SOLID SURFACES

Ranjini Devi A/P Rama

Master of Science in Mechanical Engineering

2025

HEAT TRANSPORT AND ADSORPTION MECHANISMS OF LINEAR ALKANE LIQUID ON SOLID SURFACES

RANJINI DEVI A/P RAMA

A thesis submitted
in fulfillment of the requirements for the degree of Master of Science in Mechanical Engineering

Faculty of Mechanical Technology and Engineering

UNIVERSITI TEKNIKAL MALAYSIA MELAKA

2025

DECLARATION

I declare that this thesis entitled “Heat Transport and Adsorption Mechanisms of Linear Alkane Liquid on Solid Surfaces” is the result of my own research except as cited in the references. The thesis has not been accepted for any degree and is not concurrently submitted in candidature of any other degree.

Signature :.....

Name :RANJINI DEVI A/P RAMA

Date :4/2/2025

APPROVAL

I hereby declare that I have read this thesis and in my opinion this thesis is sufficient in terms of scope and quality for the award of Master of Science in Mechanical Engineering

Signature :.....

Supervisor Name : ABDUL RAFEQ BIN SALEMAN

Date : 5 FEB 2025

DEDICATION

To my beloved mother and father.

ABSTRACT

The interaction between solid surfaces and liquid hydrocarbons known as solid-liquid (S-L) interfaces plays a crucial role in various engineering applications that determine the behaviour of liquid orientations which are referred to as adsorption mechanisms. Such interaction is commonly paired with heat transfer at S-L interfaces which are referred to as thermal transport mechanisms. These two important characters are the main contributors to the performances of the S-L interfaces system. The problem arises from the limited understanding of how liquid hydrocarbons behave on solid surfaces during operational conditions, which directly affects their adsorption mechanisms and subsequently their heat transport mechanisms efficiency. Existing studies have primarily focused on experimental methods that do not adequately capture the molecular orientations near the solid surfaces. To address this gap, this study employs nonequilibrium molecular dynamics (NEMD) simulations to analyse the adsorption mechanisms of linear liquid alkane of butane (C_4H_{10}) and pentane (C_5H_{12}) as they interact with crystal planes of Face-centered cubic (FCC) lattice of (100), (110) and (111). The methodology involves simulating the model that consists of three layers of solid - liquid – solid, with a temperature difference applied across the system to evaluate the heat flux across the systems. To address the adsorption mechanisms the structural properties namely density distributions, orientation order parameter and radius of gyration are evaluated. On the other hand the thermal transport is evaluated based on the temperature distributions and the generated heat flux as the temperature difference is applied across the systems. Molecular dynamics simulations were used to investigate how FCC crystal orientations affect the thermal and adsorption behaviour of C_4H_{10} and C_5H_{12} at solid–liquid interfaces. The (111) surface exhibited the highest first adsorption peak at 966.94 kg/m³ for C_5H_{12}, followed by (100) (801.79 kg/m³) and (110) (784.76 kg/m³), corresponding to the number of atoms per layer (224, 200, and 192, respectively). The thermal conductivity for C_5H_{12} is 6.62×10^6 for (100), 6.07×10^6 for (110) and 6.51×10^6 for (111). For C4H10 the thermal conductivity is 5.92×10^6 for (100), 6.08×10^6 for (110) and 5.69×10^6 for (111). In conclusion, C_5H_{10} has a larger adsorption mechanism and higher thermal conductivity as compared to C_4H_{10}. The findings contribute to a deeper understanding of interfacial thermal resistance and lay the groundwork for future research aimed at optimising heat transfer in engineering applications involving liquid hydrocarbons.

PENGANGKUTAN HABA DAN MEKANISME PENYERAPAN CECAIR ALKANA LELURUS PADA PERMUKAAN PEPEJAL

ABSTRAK

Interaksi antara permukaan pepejal dan cecair hidrokarbon juga dikenali sebagai antara muka Pepejal -Cecair (S-L) memainkan peranan penting dalam pelbagai aplikasi kejuruteraan yang menentukan kelakuan orientasi cecair yang dirujuk sebagai mekanisme penjerapan. Interaksi sedemikian biasanya berpasangan dengan pemindahan haba pada antara muka S-L yang dirujuk sebagai mekanisme pengangkutan terma. Kedua-dua ciri penting ini merupakan penyumbang utama kepada prestasi sistem antara muka S-L. Masalah timbul daripada pemahaman terhad tentang bagaimana cecair hidrokarbon berkelakuan berdekatan permukaan pepejal semasa keadaan operasi, yang secara langsung mempengaruhi mekanisme penyerapannya dan seterusnya, kecekapan mekanisma pemindahan haba. Kajian sedia ada tertumpu terutamanya pada kaedah eksperimen yang tidak menangkap orientasi molekul pada permukaan pepejal dengan secukupnya. Untuk menangani jurang ini, kajian ini menggunakan simulasi dinamik molekul nonequilibrium (NEMD) untuk menganalisis mekanisme penjerapan cecair alkana lelurus, butana (C_4H_{10}) dan pentana (C_5H_{12}) semasa ia berinteraksi dengan satah kekisi kiub berpusat muka (FCC), (100), (110) dan (111). Kaedahnya adalah melibatkan simulasi model yang terdiri daripada 3 lapisan pepejal – cecair – pepejal dengan perbezaan suhu dikenakan di seluruh sistem untuk menilai fluks haba merentas sistem. Untuk menangani mekanisme penjerapan sifat struktur iaitu taburan ketumpatan, parameter susunan orientasi dan jejari kilasan dinilai. Sebaliknya pengangkutan terma dinilai berdasarkan taburan suhu dan fluks haba yang dijana kerana perbezaan suhu digunakan pada system. Simulasi dinamik molekul digunakan untuk mengkaji kesan orientasi kristal FCC terhadap tingkah laku penjerapan dan terma bagi C_4H_{10} dan C_5H_{12} pada antara muka pepejal–cecair. Permukaan (111) menunjukkan puncak penjerapan pertama tertinggi iaitu 966.94 kg/m³ untuk C_5H_{12}, diikuti oleh (100) (801.79 kg/m³) dan (110) (784.76 kg/m³), seiring dengan bilangan atom dalam setiap lapisan (224, 200, dan 192). Peningkatan suhu daripada 280 K ke 360 K menyebabkan puncak menjadi kurang tajam, mencerminkan penjerapan yang lemah dan gerakan terma yang meningkat. C_4H_{10} menunjukkan nilai lonjakan suhu (TJ) yang lebih rendah berbanding C_5H_{12}; sebagai contoh, pada permukaan (110), TJ ialah 2.53 K untuk C_4H_{10} berbanding 4.17 K bagi C_5H_{12}. Antara ketiga-tiga permukaan, (110) menunjukkan nilai TJ paling rendah, menandakan kecekapan pemindahan haba yang lebih baik. Hasil ini membuktikan bahawa struktur permukaan dan saiz molekul mempengaruhi lapisan ketumpatan dan rintangan terma pada antara muka. Penemuan ini menyumbang kepada pemahaman yang lebih mendalam tentang rintangan haba antara muka dan meletakkan asas untuk penyelidikan masa depan yang bertujuan untuk mengoptimumkan pemindahan haba dalam aplikasi kejuruteraan yang melibatkan hidrokarbon cecair.

ACKNOWLEDGEMENT

I am profoundly grateful to Dr. Abdul Rafeq Bin Saleman for his exceptional mentorship, unwavering support, and profound guidance during the completion of this thesis. This research journey has been substantially influenced by Dr. Rafeq's expertise, patience, and insightful feedback. His commitment to academic excellence and his encouragement to investigate novel concepts have been instrumental in my development as a researcher. I feel incredibly privileged to have been able to learn under his guidance, and I am appreciative of his confidence in my capabilities.

Finally, I am profoundly appreciative of my late mother, whose unwavering faith in my capabilities continues to motivate me. Throughout this voyage, her support has been a guiding light, even in her absence. Because of her encouragement, I began this thesis and continue to work on it in her honor, fulfilling her aspiration for me to achieve grandeur.

I have been continually reminded of the significance of perseverance and dedication by her spirit, which has fueled my determination and strengthened my resolve. I am eternally grateful to her for instilling in me the principles of ambition and resilience.

Furthermore, I would like to express my gratitude to my family and friends for their unwavering support and understanding throughout this effort. Their support has been a source of inspiration, and their confidence in my abilities has served as an ongoing source of motivation.

TABLE OF CONTENTS

LIST OF TABLES

LIST OF FIGURES

LIST OF ABBREVIATIONS

AMM	-	Acoustic Mismatch Model
Au	-	Gold
C_4H_{10}	-	Butane
C_5H_{12}	-	Pentane
DMM	-	Diffusive Mismatch Model
EAM	-	Embedded Atom Model
FCC	-	Face Centered Cubic
LJ	-	Lennard-Jones Potential
MD	-	Molecular Dynamics
MEMS	-	Microelectromechanical Systems
NEMD	-	Nonequilibrium Molecular Dynamics
NEMS	-	Nanoelectromechanical Systems
NPT	-	Isobaric-isothermal Ensemble
NVT	-	Canonical Ensemble
PBC	-	Periodic Boundary Conditions
r-RESPA	-	Reversible Reference System Propagator
S-L	-	Solid-Liquid
TBC	-	Thermal Boundary Condition
TBR	-	Thermal Boundary Resistance
TJ	-	Temperature Jump
UTeM	-	Universiti Teknikal Malaysia Melaka

LIST OF SYMBOLS

Å	-	Angstrom
E	-	Total Energy
G	-	Time Propagator
ij	-	Between Unit Atom i and j
J	-	Heat Flux
r	-	Distance Between Two Atoms
Z	-	Acoustic Mismatch Model Impedance
Φ	-	Morse Potential Coefficient
Fl	-	Long Range Force
Fs	-	Short Range Force
ε	-	Energy Parameter for Lennard-Jones Potential
ρ	-	Density
σ	-	Size Parameter for Lennard-Jones Potential
τp	-	Relaxation Time Step for Barostat

LIST OF APPENDICES

LIST OF PUBLICATIONS

The followings are the list of publications related to the work on this thesis:

Ranjini Devi Rama, Abdul Rafeq Saleman, Muhamad Shukri Zakaria, Mohd Afzanizam Mohd Rosli, Bukhari Manshoor, 2024. Orientation of Linear Liquid Alkane on Solid Surface of Face Centered Cubic Lattice of (100), (110) and (111). *Journal of Advanced Research in Applied Mechanics (JARAM),* vol. 124, pp. 152–162, 2024. (SCOPUS indexed, Q4, IF = 0.1 (2023)

The 6th Postgraduate Research Symposium on Mechanical Engineering (PRiSME 2024) Program

CHAPTER 1

INTRODUCTION

1.1 Background

Solids interacting with liquids have been found in a wide range of engineering applications, featuring prominently in industrial systems and in the field of tribology. Important studies in this area include works by (Kumar et al., 2022; Miao et al., 2024). These interactions are also essential in the applications of thermal management systems, including thermal interface materials and active thermal systems, as highlighted by past researchers like (Cui and Cui, 2021; Feng et al., 2019; Ma et al., 2021). Unambiguously, past studies (Cui and Cui, 2021; Feng et al., 2019; Ma et al., 2021) indicate that the interfaces between solids and liquids, known as Solid-Liquid (S-L) interfaces, are exceptionally crucial for effective heat transfer. Thus, understanding the dynamics of heat transport at the S-L interfaces is essential for the development of advanced engineering systems.

In recent years, due to rapid advancements in nanotechnology (Fujiwara and Shibahara, 2019; Qian et al., 2018), researchers have been drawn to the exploration of molecular-level research in the fields of magnetic memory, quantum information, medical diagnostics and catalysis. Among these areas of interest lies the investigation of heat transport at solid-liquid (S-L) interfaces. At the molecular level, the underlying principles governing such systems are often intricate and defy conventional macroscopic understanding. To solve the problem a the molecular-level, Molecular Dynamics (MD) simulation has emerged as a pivotal tool capable of capturing molecular-scale phenomena. The previous studies examining interfacial thermal resistance at the S-L interfaces, (Anandakrishnan and Sathian, 2023; Klochko et al., 2023; Matsubara et al., 2023; Zhang et

al., 2023) suggest that atomic-scale structures are crucial for thermal transport and surface coatings. Additionally, the researchers also indicate the discrepancy of approximately 10% between experimental and MD simulated systems. Consequently, MD simulation is regarded as a valuable tool for reproducing molecular-scale phenomena, and facilitating detailed analysis in this area.

Past research has elucidated that the dynamics of heat transport at (S-L) interfaces are intricately tied to the Interfacial Thermal Resistance (ITR) also named as Thermal Boundary Resistance (TBR), which is a measure known to encapsulate thermal resistance stemming from the combination of solid and liquid phases alongside disparities in interaction forces (Giri et al., 2023; Wang et al., 2022). The term Kapitza resistance, quantifies thermal resistance at S-L interfaces, which results from temperature discrepancies or temperature jumps (TJ) occurring at these boundaries (Ghatage et al., 2020). The interfacial thermal resistance dates to 1941, and is credited to Kapitza's investigations into the measure of thermal resistance at (S-L) interfaces.

Typically, interfacial thermal resistance is discussed in terms of thermal boundary resistance (TBR). Predictive models such as the acoustic mismatch model (AMM) and diffusive mismatch model (DMM) have been developed to understand heat transport, focusing on scattering of phonon at the interfaces (Ghatage et al., 2020; Song et al., 2022). The AMM assumes a perfectly geometrical interface with elastic phonon transfer throughout, while the DMM posits diffusive scattering at interfaces, accounting for precise interface roughness. However, at the molecular level, interfacial thermal resistance is primarily governed by molecular interactions between solid and liquid phases (Ghatage et al., 2020). Recent studies have significantly advanced our understanding of heat transport at S-L interfaces through investigations into interfacial thermal resistance (Anandakrishnan and Sathian, 2023).

Over recent years, extensive research efforts have been directed towards comprehending the mechanisms underlying heat transport across (S-L) interfaces, focusing on the principles of thermal energy and adsorption mechanisms (H. Wu et al., 2023). Numerous studies have explored aspects related to thermal energy (Saleman et al., 2021) and liquid adsorption orientation (Guo et al., 2019b; Qian et al., 2018) at S-L interfaces, often considering the interfacial thermal resistance. On the other hand, several investigations have examined adsorption mechanisms of liquid hydrocarbons on solid surfaces and heat transport at the solid-liquid interface (Fujiwara and Shibahara, 2019; Guo et al., 2019b, 2019a). However, these studies typically focused on the molecular dynamics that investigate the effects of surfactant adsorption on heat transfer at solid-liquid interfaces and atomic-scale thermal manipulation with adsorbed atoms on solid surfaces at liquid-solid interfaces, which neglect to utilize the Face Centered Cubic (FCC) structures with liquid adsorption in their simulations. Consequently, while studies by (Chang et al., 2019) contribute to understanding thermal resistances and evaporator thermal conductivities in thin vapor chambers, but they overlook the impact of adsorption mechanisms of liquid hydrocarbons on solid surfaces and heat transport at the solid-liquid interface. Thus, research on adsorption mechanisms of liquid hydrocarbons on solid surfaces and heat transport at the S-L interface from crystal planes (100), (110), (111) remains limited.

1.2 Problem Statement

S-L interfaces involving solid surfaces coming into contact with long hydrocarbon liquids have been found in numerous applications across various engineering systems. The investigation of transport properties near S-L interfaces encompasses the comprehension of adhesion (Zhang et al., 2021), wetting (Yu et al., 2019), and lubrication (Liu et al., 2021). Although, a significant effort has been devoted to characterising adsorption mechanisms

using experimental methods that involve examining wear and friction at contact interfaces (Chen and Qian, 2021), the exact behaviour and orientation of liquid on solid surfaces during system operation, which directly influences adsorption mechanisms, remains unclear. Thus, the aim of the study is to investigate the adsorption mechanisms of liquid hydrocarbons on solid surfaces using Non- Equilibrium Molecular Dynamics (NEMD) simulations, focusing on structural quantities such as density distributions, orientational order parameter, and radius of gyration. Furthermore, since the effects of the adsorption mechanisms are often reflected by heat transport across the liquid and solid the correlation of the structural quantities and the heat transport across the liquid and solid will be elaborated.

1.3 Research Question

i). What are the adsorption mechanisms of liquid hydrocarbons (C_4H_{10} and C_5H_{12}) on solid surfaces, and how can they be characterised using structural quantities such as density, orientation order parameter, and radius of gyration?

ii). How does interfacial thermal resistance (TBR) influence heat transport at solid-liquid interfaces?

1.4 Research Objective

The main objective of this investigation is to clarify the factors that influence the characteristics of adsorption mechanisms and heat transport mechanisms at the S-L interfaces.

i). To clarify the adsorption mechanisms of various liquid hydrocarbons on solid surfaces using molecular dynamics simulations, by examining the structural quantities which are density, orientation order parameter, and radius of gyration.

ii). To identify the heat flux at the contact interfaces of S-L, based on the temperature discontinuity at the interfaces and thermal boundary resistance.

1.5 Scope of Research

The scope is determined by the objective of this investigation. The simulation model that will be examined in this study is a straight-line liquid butane (C_4H_{10}) and pentane (C_5H_{12}) that has been enclosed between two parallel solid walls. The methodology section will provide further details. To examine the effects of the solid's surface structure, the crystal plane of the face-centered cubic (FCC) structure, which is (100), (110), and (111) will be employed for the two parallel solid walls. This research employs a simulation method to clarify the heat transfer at the S-L interfaces. It is designed to examine the adsorption mechanisms of various liquid hydrocarbons on solid surfaces by means of molecular dynamics simulations. The research concentration is on the examination of structural properties, including density, orientation order parameter, and radius of gyration. The liquids, which are composed of (C_4H_{10}) and (C_5H_{12}), will be employed in this paper to ensure that additional factors, such as molecular diameters and length, are eradicated from the investigation. In this investigation, the thermal boundary resistance (TBR) at the solid–liquid interfaces will be evaluated by analysing the heat flux, in order to determine the interfacial

thermal resistance between the solid and liquid phases. The temperature will be varied throughout the simulation system in this investigation, utilising the nonequilibrium molecular dynamics (NEMD) simulation.

1.6 Significance of study

This research represents a crucial effort to deepen our understanding of molecular interactions at solid–liquid interfaces, with a particular focus on the complex mechanisms of heat transfer and adsorption. The significance is both broad and multifaceted, offering valuable contributions across several critical areas of engineering and materials science. First, this study advances the design and optimisation of lubrication systems, cutting tools, and thermal interface materials by developing a comprehensive simulation model for S-L interfaces. This model will enable the precise characterisation and prediction of interfacial behaviour, providing a strong foundation for engineering advances in these fields. Second, by exploring the molecular dynamics of thermal transport and adsorption phenomena, this work aims to reveal fundamental insights into how these processes occur and evolve at the nanoscale. Such knowledge is vital for manipulating material interfaces to optimise thermal and adhesive properties, opening new pathways for innovations in nanotechnology and precision engineering. Finally, by generating novel insights into the interactions between liquid hydrocarbons and solid surfaces and their collective influence on thermal behaviour, this research directly addresses pressing technological challenges. Its outcomes have the potential to transform tribology and materials engineering, making a significant contribution to the design of next-generation materials and devices. In doing so, this work not only fills existing knowledge gaps but also paves the way for future breakthroughs in engineering and material development.

1.7 Thesis Outline

This work primarily focuses on heat transport at solid-liquid interfaces; specifically, this study employs molecular dynamics simulations to investigate the adsorption mechanisms of liquid hydrocarbons on solid surfaces. The focus is on analysing structural features such as density, orientational order parameter, and radius of gyration. Additionally, the study examines the association between these variables and heat transport at solid-liquid interfaces on the crystal planes of (100), (110), and (111). The simulation focuses on two types of liquids at solid-liquid (S-L) interfaces. The structure of this study is as follows:

- Chapter 1 provides an overview of the S-L interface, including an introduction and a review of previous studies. This material is aimed at gaining a general understanding of the adsorption mechanisms of liquid hydrocarbons and heat transport at the S-L interface.
- Chapter 2 involves conducting a preliminary study and researching the literature review to gather information on the historical and methodological aspects relevant to this study. This will enable a more comprehensive understanding of the theoretical framework.
- Chapter 3 outlines the methodology used in this study, including the application of constant velocity to the solid walls. These elements are used to model the S- L interface between solid gold (Au) and the simple alkane liquids, butane (C_4H_{10}). and pentane (C_5H_{12}). This chapter will provide an explanation of the simulation condition for this model, as well as a clarification and discussion of the validation of the simulation system.
- Chapter 4 provides data and details necessary for understanding heat transport

direction. The data will be analysed for density distribution, radius of gyration, orientation order parameter, temperature distribution, heat flux, and interfacial thermal resistance, which will be further explained in this chapter.

- Chapter 5 describes the conclusion of this study, and the summary of the results is explained in detail.

CHAPTER 2

LITERATURE REVIEW

2.1 Introduction

Molecular dynamics (MD) simulation has become a critical tool for investigating nanoscale interfacial phenomena, particularly at S-L interfaces. Recent advancements have expanded its use beyond theoretical fundamentals, enabling detailed studies of adsorption mechanisms, thermal boundary resistance (TBR), and molecular orientation of hydrocarbons on solid surfaces. However, despite the wealth of studies on MD fundamentals, there remains a gap in comprehensive research addressing how FCC surface orientation and alkane chain length jointly affect heat transfer and molecular behaviour. This chapter reviews recent literature. The chapter will provide the simulation model, potential functions, and thermal boundary resistance to establish the MD simulation framework for the current study.

2.2 Molecular Dynamics Simulations of S-L Interfaces

S-L interface modeling has seen significant development in recent years, especially in the context of nanoconfined fluids and thermal transport (Anandakrishnan and Sathian, 2023; Zhang et al., 2025). Traditional studies often model metallic surfaces such as FCC (100), (110), and (111) planes to examine how surface morphology affects fluid behaviour. Recent molecular dynamics simulations have confirmed that crystal orientation significantly influences interfacial heat transfer and structuring. For instance, simulations of n-alkane fluids at different crystal planes have demonstrated distinct layering, orientation alignment, and energy transport depending on surface orientation and fluid chain length (El-Rifai et al., 2024a). However, most of the current studies focus on generic Lennard-Jones fluids or

monatomic systems. The Lennard-Jones (LJ) 12-6 potential is classically decomposed into two parts: a steep short-range repulsive, modeling Pauli exclusion, and a smoother long-range attractive term, representing London dispersion forces. This functional form remains foundational in molecular dynamics force fields and is widely applied for modeling non-bonded interactions in simple liquids and alkanes (Harrison et al., 2018; Saleman et al., 2025) as shown in Equation (2.1)

$$V(r_{ij}) = 4\varepsilon_{ij}\left[\left(\frac{\sigma_{ij}}{r_{ij}}\right)^{12} - \left(\frac{\sigma_{ij}}{r_{ij}}\right)^{6}\right] \quad 2.1$$

Moreover, the confinement of liquids between solid walls leads to distinct molecular arrangements and altered phase behaviour compared to bulk conditions. These confinement effects significantly influence transport properties and molecular layering near the interface (Zou et al., 2021). Advances in high-resolution simulations now allow for precise characterization of these layers, offering insights into the interfacial thermodynamics of nanoconfined systems (Schmitt et al., 2022).

Despite numerous studies modeling interfacial phenomena using Lennard-Jones fluids or monatomic systems, there is a notable lack of work that examines the combined effects of hydrocarbon chain length variation and FCC surface orientation (100), (110), and (111) in nanoconfined environments. This gap is particularly evident in the context of molecular layering, orientation ordering, and interfacial heat transfer mechanisms. Therefore, a detailed molecular dynamics investigation that considers both realistic molecular structure and crystal orientation is essential to better understand interfacial transport phenomena relevant to nanoscale thermal management applications.

2.3 Potential Functions and Interatomic Forces

2.3.1 Solid Interaction forces

There are a bundle of interaction forces that have been investigated and utilized even in recent studies namely are Morse potentials, Lennard Jones, Eam, and many more. A variety of interatomic potentials have been developed and applied to model interaction forces in molecular simulations, each tailored to specific materials and physical conditions. For instance, the Lennard–Jones potential has been extensively employed to describe van der Waals interactions and noble gas systems due to its simplicity and reasonable accuracy for weakly interacting species. The Embedded Atom Method (EAM) is widely used for metallic systems as it incorporates the many-body effects arising from electron density contributions, making it highly effective for modeling bulk metals and alloys. The Morse potential, on the other hand, is often utilised to capture the anharmonic behaviour of bonded interactions, particularly in systems where bond stretching and dissociation are relevant, offering flexibility in modeling both short- and long-range interactions.

In this study, the focus is placed on liquid systems with comparatively less emphasis on solid phases. The Morse potential is selected as it provides satisfactory accuracy in reproducing interatomic forces in liquid environments and aligns well with experimental observations reported in prior works. Its ability to represent both attractive and repulsive interactions in a smooth, physically meaningful manner makes it a suitable choice for investigating the thermophysical behaviour of the studied system.

Accurate potential functions are essential for simulating realistic interfacial behaviour. Morse-type potentials remain widely used for modeling gold and similar FCC metals due to their ability to capture anharmonic interactions and tunable parameter flexibility (Aldossary and Al Rsheed, 2020; Peterson and Russell, 2025). The Equation (2.2) is the Morse potential is covered in this study:

$$\Phi(r_{ij}) = D\ [e^{-2\alpha(r_{ij}-r_o)} - 2e^{\alpha(r_{ij}-r_o)}] \quad 2.2$$

The term r_{ij}represents the distance between the two atoms. The term D represents the well depth, which is the measure of potential energy in a diatomic molecule. r refers to the equilibrium distance between the atoms. The term a refers to the stiffness of the interaction, which is used to regulate the width of the potential.

2.3.2 liquid Interaction forces

In previous studies, liquids have been modeled using various molecular representations, including the United Atom (UA)(Knudsen et al., 2024), All Atom (AA)(Oliveira et al., 2022), and Anisotropic United Atom (AUA)(Castro Anaya et al., 2023) approaches, among others. In the UA approach, groups of atoms typically non-polar hydrogen atoms bonded to carbons are represented as a single interaction site, thereby reducing the number of interaction centers and computational cost (McCready et al., 2024). The AA approach, in contrast, explicitly represents every atom in the molecule, offering higher structural detail at the expense of increased computational demand (Smardz et al., 2024). The AUA approach improves upon UA by shifting the center of interaction sites to more accurately represent the anisotropy of molecular geometry and interactions (Mutoru et al., 2013).

In recent studies, UA, AA, and hybrid force fields continue to evolve for liquid-phase modeling. Recent research has been found that enhanced the OPPES UA model by optimizing it for associating fluids such as alcohols and glycols improving predictions of vapor–liquid equilibria (Jang et al., 2025). Efforts to directly compare UA and AA representations highlight the significant trade-offs in resolution and efficiency. More specialized UA parameterization notably for hydrocarbon systems demonstrates adaptability in complex environments like bituminous materials (Assaf et al., 2024). On the AA side, the

updated OPLS force field shows substantial accuracy gains over conventional OPLS-AA across branched and long-chain alkanes (Ghahremanpour et al., 2022). Additionally, fine-tuning OPLS-AA for ethanol leads to notably improved diffusion behaviours, underscoring the importance of parameter adjustments in capturing liquid dynamics (Zêzere et al., 2023).

From these investigations, the UA–NERD potential has emerged as a particularly promising choice, offering a practical balance between computational efficiency and accuracy in reproducing both structural and thermophysical properties. Its reduced number of interaction sites compared to AA models allows for faster simulations, while its parameterization retains the ability to capture key molecular interactions relevant to liquid-phase studies.

For hydrocarbon liquids, the united-atom NERD potential offers computational efficiency while preserving physical accuracy NERD describes CH_x groups as single interaction sites with good fidelity in hydrocarbon liquids (Ito et al., 2022) comparative studies show NERD often matches or outperforms all-atom models in reproducing liquid-phase density and viscosity, while being far less computationally demanding (da Silva et al., 2022; Math et al., 2022) reported that recent improvements in bonded and non-bonded interaction parameters have enhanced the prediction of liquid conformations at interfaces. Additionally, Lorentz-Berthelot combining rules are still commonly applied for cross interactions between solid and liquid phases, validated in studies by (J. Wu et al., 2023; Yu et al., 2023).

2.3.3 Summary of potential functions for solid and liquid

(Wilson et al., 2022) Although Morse-type potentials for FCC metals and NERD united-atom models for hydrocarbons are well-established independently, there is a notable lack of integrated studies that evaluate the combined applicability of these models at solid–

liquid interfaces, particularly under nanoscale confinement and varying temperature conditions. The validity of the Lorentz–Berthelot combining rules for such varied systems especially involving gold surfaces and hydrocarbon chain variations (C_4H_{10} and C_5H_{12}) has not been fully assessed in the context of interfacial heat transfer and molecular layering. This gap presents an opportunity to develop a strong molecular dynamics framework that leverages the strengths of Morse and NERD potentials to gain quantitative insight into the structural and thermal behaviour of confined solid–liquid systems.

2.4 Simulations of Molecular Dynamics

In recent years, molecular dynamics (MD) simulations have significantly advanced the modeling of microscopic systems in nanoscience, materials science, and interfacial phenomena. MD simulations provide critical insights into the structural, thermodynamic, and dynamic properties of molecular systems across various spatial and temporal scales, capturing detailed atomic-scale interactions and molecular behaviours that are often inaccessible through experimental techniques such as scanning probe microscopy or spectroscopy (Islam et al., 2025; Jiang et al., 2025).

Modern MD simulations have become crucial in studying physicochemical processes, ranging from adsorption and diffusion to thermal transport at interfaces (Anandakrishnan and Sathian, 2023). By modeling atomistic motion using interatomic potentials and Newtonian mechanics, MD enables exploration of molecular interactions over time, facilitating the prediction of both equilibrium and non-equilibrium properties (Wan et al., 2023).

These include heat transfer at solid–liquid interfaces, orientation-dependent molecular adsorption, and confinement effects within nanostructures. For instance, (Schmitt et al., 2022) conducted a detailed MD study of heat transfer across solid–fluid interfaces

using a Lennard-Jones model system, introducing the concepts of Kapitza length and a dimensionless Kapitza interface number to quantify the effects of interaction strength, channel width, and fluid density on interfacial heat transport. In a related investigation, (Luo et al., 2024a) examined the influence of surface roughness and polymer chain length on interfacial thermal resistance at solid–liquid interfaces. Their findings highlighted that the molecular orientation and chain length of polymers, analogous to alkanes, significantly affect heat transfer through changes in the interfacial structure.

However, there remains a notable gap in studies that simultaneously explore the combined influence of surface orientation, alkane chain length, and thermal boundary resistance, particularly in systems involving hydrocarbons interacting with FCC crystal planes. This thesis aims to bridge that gap by providing detailed atomistic insight into how these parameters jointly influence interfacial thermal transport (Silvestrelli, 2023; Zhang et al., 2023).

2.4.1 Basic Principles of Molecular Dynamics (MD) Simulation

Molecular Dynamics (MD) Simulation is rooted in computational chemistry, offering a dynamic methodology to observe the evolution of molecular interactions over space and time. MD simulation is a computational chemistry method that tracks and temporal evolution of interacting molecules, providing insights into the movements of atoms and molecules based on the equations of motion. Typically, MD simulations translate microscopic trajectories of particles into macroscopic quantities. The simulation's trajectory, generated by integrating Newton's equations of motion for the MD system, outlines the positions and velocities of molecules over time and space, offering detailed insights into molecular interactions.

2.4.2 Fundamental Theory of Molecular Dynamics

In MD simulations, the system's total energy is described using the Hamiltonian function, which combines kinetic and potential energy terms:

$$H(r,p) = K(p) + V(r) \tag{2.3}$$

$$K(p) = \sum_{i}^{n} \frac{P_i^2}{2m_i} \tag{2.4}$$

Where $H(r,p)$ is the total energy of function of generalized coordinates, P_i and generalized momentum, r_i. $K(p)$ is kinetic energy and $V(r)$ is potential energy of interaction between particles. m_i is mass of atom i. n is number of particles of coordinates, p, and momentum, With the time derivatives of positions and momenta are given by Hamiltonian equation (2.5) can express as:

$$\dot{r_i} = \frac{\partial H}{\partial p_i}, \dot{p_i} = -\frac{\partial H}{\partial r_i} \tag{2.5}$$

The momentum $\dot{r_i}$ and coordinate, $\dot{p_i}$ are refer as the function of time derivative, $f(t)$ which equation (2.6):

$$iLf(t) = \frac{df(t)}{dt} \tag{2.6}$$

Where the equation (2.7) of iL can be written as below:

$$iL = \sum_i \dot{r}_i \frac{\partial}{\partial r_i} + \sum_i \dot{p}_i \frac{\partial}{\partial p_i} i \quad (2.7)$$

This Hamiltonian formulation allows MD simulations to compute the evolution of molecular systems through time by integrating Newton's equations of motion. These equations generate routes that describe how particles move in phase space, a multidimensional space defined by the combination of all particle coordinates and momenta (Zhang et al., 2023).

The concept of ergodicity is essential in MD. In ergodic systems, the time average of a property is equivalent to its ensemble average, ensuring that the simulation adequately samples phase space. However, many real systems, especially at the nanoscale, exhibit non-ergodic behaviour, where phase space is not fully explored due to constraints or energy barriers (Zeng et al., 2022). This presents a challenge for nanoscale interfacial heat transfer simulations, where molecular ordering and confinement may restrict phase space sampling a gap that this thesis seeks to investigate in alkane solid interfaces.

Although molecular dynamics (MD) simulations have proven instrumental in modeling interfacial heat transport, most existing studies rely on simplified Lennard-Jones fluids or monatomic systems that fail to represent the complexity of real S-L interfaces. There remains a significant gap in the literature regarding the combined influence of alkane chain length variation and FCC crystal surface orientation on interfacial thermal transport, especially under nanoscale confinement. Furthermore, the validity of using Morse–NERD potential combinations, alongside classical assumptions of ergodicity, has not been fully examined in such systems. This thesis addresses these gaps by investigating how molecular ordering, energy transport, and phase space sampling are affected by these interdependent factors providing deeper insights into nanoscale thermal boundary resistance and the mechanisms governing solid–liquid interfacial conduction.

2.5 Molecular Dynamics' Numerical Integration Algorithm (MD)

In molecular dynamics (MD) simulations of complex systems such as solid–liquid interfaces, the reversible Reference System Propagator Algorithm (r-RESPA) has gained recognition as an efficient and accurate multiple time-step integrator. This algorithm separates forces based on their characteristic time scales short-range forces like bonded interactions are computed at fine time intervals, while long-range forces such as van der Waals or electrostatics are evaluated less frequently thus significantly reducing computational cost without compromising the accuracy of phase space trajectories or energy conservation (Martin., 2024). Recent developments have further optimized r-RESPA for high-performance simulations involving two- and three-body interactions, demonstrating its stability and efficiency in large-scale atomistic systems.

However, there remains a notable research gap concerning the application of r-RESPA in simulations involving interfacial systems, particularly those combining metallic FCC surfaces with hydrocarbon molecules. While the algorithm is well-established for homogeneous systems, its stability, time-step tuning, and thermodynamic accuracy remain underexplored in heterogeneous environments where molecular adsorption and orientation at the interface critically influence heat transport. Moreover, no recent studies have systematically assessed how variations in surface orientation and alkane chain length affect the efficiency and reliability of r-RESPA in predicting thermal boundary resistance. Therefore, this thesis seeks to address these gaps by applying and evaluating the r-RESPA algorithm in MD simulations of hydrocarbon interactions with FCC metal surfaces, focusing on optimizing time-step schemes for accurate modeling of interfacial adsorption dynamics and nanoscale heat transfer.

2.5.1 Verlet Algorithm

In molecular dynamics (MD) simulations, the Verlet algorithm remains a cornerstone for integrating Newton's equations of motion due to its simplicity, time-reversibility, symplectic structure, and energy conservation over long trajectories. It is derived by summing forward and backward Taylor expansions of positions around time *t*, thereby eliminating odd-order error terms as given in equation below:

$$r(t+\delta t) = r(t) + \frac{dr(t)}{dt}\delta t + \frac{1}{2}a\delta t^2 + \frac{1}{6}\frac{d^3}{dt^3}\delta t^3 \tag{2.8}$$

$$r(t-\delta t) = r(t) - \frac{dr(t)}{dt}\delta t + \frac{1}{2}a\delta t^2 - \frac{1}{6}\frac{d^3}{dt^3}\delta t^3 \tag{2.9}$$

Where equation is the velocity of coordinate $r(t)$, a is the acceleration of coordinate $r(t)$, and $\frac{d^3r(t)}{dt}$ is the third derivative of coordinate $r(t)$. By adding the two expressions Eq. (2.8) and (2.9) above, the basic form of Verlet algorithm will be expressed as given below:

$$r(t+\delta t) = 2r(t) - r(t-\delta t) + a(t)\delta t^2 \tag{2.10}$$

The value $a(t)$ is from the Newton's second law equation of motion where the force is the functions of coordinate $r(t)$ as given equation (2.11) below:

$$a(t) = -\left(\frac{1}{m}\right)\nabla V(r(t)) \tag{2.11}$$

Where m is the mass of particle, and $\nabla V(r(t))$ is force that represent as the function of coordinate $r(t)$.

The method efficiently computes future positions based on current and previous positions without explicitly calculating velocities, which can then be retrieved post hoc if needed. While velocity is not directly produced, kinetic energy metrics can be deduced or adapted via extended versions like velocity-Verlet or leap-frog integrators (Vyas et al., 2024).

Recent reviews reaffirm that standard Verlet integration remains robust and efficient for MD simulations in a range of systems, from biological molecules to condensed matter models (Khoshkalam, n.d.; Laurent., 2019).

2.5.2 Leap-Frog Algorithm

In molecular dynamics simulations, the Leap-Frog integrator is widely used to compute particle trajectories by interleaving velocity and position updates. Velocities are calculated at half-time-step intervals, while positions are updated at full time steps using these mid-point velocities. This structure eliminates the need for explicit velocity derivatives in the standard Verlet formula and yields trajectories equivalent to those generated by the Verlet or Velocity-Verlet schemes, but with simpler staging and lower computation overhead per time step (Goga et al., 2021). Specifically, the equation (2.12) and (2.13) given as:

$$r(t+\delta t) = r(t) + v\left(t+\frac{1}{2}\delta t\right)\delta t \tag{2.12}$$

$$v\left(t+\frac{1}{2}\delta t\right) = v\left(t-\frac{1}{2}\delta t\right) + \left(\frac{1}{m}\right)F(t)\delta t \tag{2.13}$$

Where $r(t)$ is the coordinate of particle, v is velocity, $\left(\frac{1}{m}\right)$) $F(t)$ is the acceleration of time step, and ởt is the size of time step. By substitute the Eq. (2.12) into Eq. (2.13), the Leap- Frog algorithm can be expressed as given equation below:

$$r(t+\delta t) = r(t) + \left[v\left(t+\frac{1}{2}\delta t\right) + \left(\frac{1}{m}\right)F(t)\delta t\right]\delta t \tag{2.14}$$

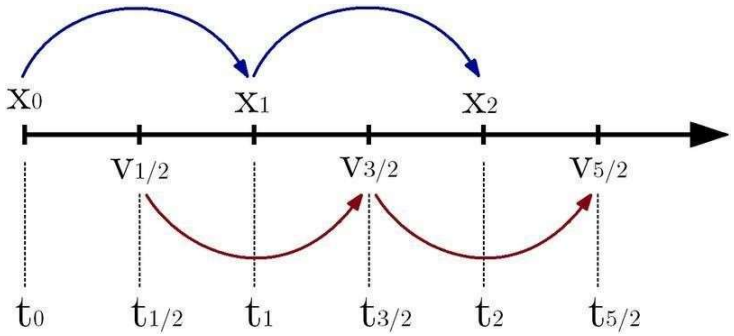

Figure 2.1 Illustration of Leap-Frog algorithm (Gisbert and Piovella, 2020)

2.5.3 Velocity-Verlet Algorithm

Velocity-Verlet algorithm most used to generate sequence of snapshot for the coordinate and velocities of particles in time interval. In general Velocity-Verlet algorithm is quite same to Leap-Frog algorithm in determining the coordinates and velocities of particles of time interval in MD simulation (Ciccotti et al., 2025; Toxvaerd, 2024). The different of Velocity- Verlet algorithm from Leap-Frog algorithm is the coordinate and velocities are calculated at similar time variables. To determine the coordinate and velocities of time interval in Velocity-Verlet algorithm as given equation below:

$$r(t+\delta t) = r(t) + v\,(t)\delta t + \left(\frac{1}{2m}\right)F(t)\delta t^2 \tag{2.15}$$

$$r(t+\delta t) = v(t) + \left(\frac{1}{2m}\right)[F(t) + F(t+\delta t)]\delta t \tag{2.16}$$

Where $r(t)$ is coordinate of particles, $v(t)$ is velocity, and $\left(\frac{1}{m}\right)F(t)$ is acceleration of time step. The Velocity-Verlet algorithm is used in the MD simulation based on the stability of time

interval, accuracy and simplicity.

2.5.4 Beeman's Algorithm

In molecular dynamics (MD) simulations, Beeman's algorithm serves as a higher-order enhancement of the Verlet integration scheme, offering identical position updates but more accurate velocity estimates via a predictor–corrector formulation. The integration formulas take into account both current and previous accelerations to achieve third-order precision in velocities and fourth-order in positions. Beeman's algorithm was published in direct development with communication between Beeman by Schofield (Schofield, 1973). Beeman's algorithm is straight development in third-order method of algorithm and refer as multi-step method (Beeman, 1976). E.g. (2.17) and Eq. (2.18) below show the right coordinate and velocities by replicate twice the differential equation to obtain acceleration:

$$r(t+\delta t) = r(t) + v\,(t)\delta t + \frac{2}{3}a(t)\delta t^2 - \frac{1}{6}a(t-\delta t)\delta t^2 \tag{2.17}$$

$$v(t+\delta t) = v(t) + v\,(t)\delta t + \frac{1}{3}a(t)\delta t^2 + \frac{5}{6}a(t)\delta t - a(t+\delta t)\delta t \tag{2.18}$$

Where $r(t)$ is coordinate at time interval, $v(t)$ is velocity of time interval, and $a(t)$ is the acceleration of time interval. Beeman's algorithm offers greater precision in velocity estimates and better energy conservation at the cost of moderate additional memory to track prior accelerations (Zhou et al., 2023).

2.5.5 r-RESPA

The r-RESPA (Reversible Reference System Propagator Algorithm) is a key time-stepping method used in molecular dynamics (MD) simulations to efficiently progress the system's state over time. Primarily, it differentiates between short-range and long-range

forces, treating the former as reference system forces while precisely calculating only the velocities for the final. This distinction allows for more rapid simulations, particularly beneficial for larger systems requiring extensive computation (Abreu and Tuckerman, 2021). The algorithm employs a single time step approach to speed up simulations, utilizing the Liouville operator to adjust reference system forces and incorporating slow variations of long-range forces into its calculations as shows below eq. (2.19),

$$iL = \sum_i \dot{r} \frac{\partial}{\partial r_i} + \sum_i F_s(r) \frac{\partial}{\partial p_i} + \sum_i F_l(r) \frac{\partial}{\partial p_i} = iL_s + \sum_i F_l(r) \frac{\partial}{\partial p_i} \tag{2.19}$$

In the r-RESPA algorithm, the time propagator is associated with the lengthy variation of the long-range force, $F_s(r)$, which is incorporated as a factor in the equation below. Here, $F_l(r)$ define the force from the reference system, representing the short-range force, while $F_l(r)$ signifies the long-range force.

$$G_{|s|}(\Delta t) = e^{\left(\frac{\Delta t}{2}\right) F_l(r) \partial/\partial p} . e^{iL_s \Delta t} . e^{\left(\frac{\Delta t}{2}\right) F_l(r) \partial/\partial p} \tag{2.20}$$

The $G_{|s|}$ molecular dynamics, could represent the time propagator or Green's function, the application of Trotter factorization specifically addresses the treatment of short- range forces within the simulation. By carefully selecting the division of the time step (Δt/n), r-RESPA maintains accurate system dynamics.

$$e^{iL_s \Delta t} = \left[e^{\left(\frac{\delta t}{2}\right) F_s(r) \partial/\partial p} . e^{\delta t r \partial/\partial r} . e^{\left(\frac{\delta t}{2}\right) F_s(r) \partial/\partial p} \right] n \tag{2.21}$$

Where in At/n, the n is selected as the suitable value to maintain the dynamics in a system. By substituting the middle propagator in Eg. (2.21) into time propagator in Eq.

(2.22), the overall propagator will be written as equation below:

$$G_{|s|}(\Delta t) = e^{\left(\frac{\Delta t}{2}\right)F_l(r)\partial/\partial p} \cdot \left[e^{\left(\frac{\delta t}{2}\right)F_s(r)\partial/\partial p} \cdot e^{\delta t r\dot{\partial}/\partial r} \cdot e^{\left(\frac{\delta t}{2}\right)F_s(r)\partial/\partial p}\right]^n \cdot e^{\left(\frac{\Delta t}{2}\right)F_l(r)\partial/\partial p} \quad (2.22)$$

The previous value of long range force, F1(r) and short range force, F,(r) are used to be the input for the following step to determine the force. The calculation of force, F() in r-RESPA algorithm is shown as equation below:

$$F(r) = F_s(r) + F_l(r) \quad (2.23)$$

While many previous MD studies have successfully applied single time-step algorithms like Verlet or Velocity-Verlet for equilibrium simulations, few have implemented r-RESPA in non-equilibrium simulations of thermal transport across S-L interfaces, especially when considering anisotropic surfaces like FCC (100), (110), and (111). Furthermore, the combined study of chain-length-dependent adsorption behaviour, orientation ordering, and thermal boundary resistance using r-RESPA is still underexplored in the literature (Chen et al., 2023; Zeng et al., 2022). Most current works use standard integrators without leveraging the efficiency of multiple time-step schemes, especially for confined hydrocarbon systems interacting with crystal surfaces.

In the r-RESPA method, forces are categorized based on their range of influence, short-range forces, denoted as $F_s(r)$ and $F_l(r)$ long-range forces. In the r-RESPA algorithm utilised for molecular dynamics (MD) simulations, forces are divided into short-range and long-range categories. This function acts as a cubic spline, transitioning smoothly from one at close inter-particle distances to zero at greater distances, effectively distinguishing between the two types of forces. The formulation ® allows for a seamless integration of short-range and long-range forces optimizing computational efficiency.

$$F(r) = s(r)F(r) + (1 - s(r))F(r) = F_s(r) + F_l(r) \quad (2.24)$$

Particularly, short-range force calculations are less CPU-intensive as they involve interactions with nearby cells, and by adjusting velocities and coordinates on separate timescales, the algorithm enhances computational efficiency without compromising accuracy.

2.5.6 Summary of computational algorithm

While the r-RESPA (Reversible Reference System Propagator Algorithm) has proven effective for large-scale molecular simulations by separating short- and long-range force evaluations, its application in heterogeneous interfacial systems, particularly those involving hydrocarbons interacting with FCC crystal plane surfaces, remains poorly explored. Most studies of interfacial thermal transport still rely on standard single time-step integrators such as Verlet or Velocity-Verlet, overlooking the computational and temporal efficiency benefits offered by r-RESPA in complex systems. Furthermore, there is no existing systematic study that applies r-RESPA to evaluate the coupled effects of FCC crystal orientation, alkane chain length, and confinement-induced molecular ordering on thermal boundary resistance. This thesis aims to fill this gap by implementing and optimizing r- RESPA for solid–liquid interface modeling, focusing on time-step stability, force decomposition, and the impact on heat transport and interfacial dynamics in confined hydrocarbon systems.

2.6 Measurement of molecular dynamics

Molecular dynamics (MD) simulations offer powerful methods to quantify atomic and molecular behaviour under various conditions. Recent studies have expanded the use of MD to measure interfacial properties, thermal transport, and molecular ordering, especially at S-L interfaces (Chen et al., 2022; Schmitt et al., 2022). In this research, a combination of

measurement techniques is used to evaluate the thermal and structural behaviour of (C_4H_{10}) and (C_5H_{12}) in contact with face-centered cubic (FCC) gold surfaces (100), (110), and (111). These methods provide insights into heat transfer mechanisms and adsorption phenomena at the molecular level. The key properties investigated include density distribution profiles, radius of gyration, orientation order parameter (OOP), heat flux calculations, and thermal boundary resistance (TBR).

These measurements are critical in assessing the heat enhancement and adsorption behaviour at S-L interfaces, particularly in systems where the surface structure and alkane chain length influence interfacial dynamics (Chen et al., 2023).

2.6.1 Density distribution

In molecular dynamics (MD) studies, density distribution profiles serve as a powerful tool to elucidate how molecules organize near solid interfaces revealing adsorption layers and oscillatory behaviour depending on confinement and surface interactions. For linear alkanes, MD simulations of hydrocarbons near carbonaceous and metallic surfaces show pronounced layering effects that depend strongly on chain length longer molecules like n-hexadecane display stronger and more extended density oscillations compared to shorter, branched alkanes (Corral-Casas et al., 2025; Tian et al., 2022). Additionally, mixed alkane systems under confinement exhibit clear density stratification varying with molecular size and film thickness longer-chain species forming sharper peaks closer to the surface (Du et al., 2020). These methods compute local number density by counting molecules (or pseudoatoms) in defined slab volumes and convert these to mass density using known molar mass and Avogadro's constant.

2.6.2 Radius of Gyration

The radius of gyration (Rg) is used to evaluate molecular conformation and compactness, especially for flexible molecules near interfaces. It is defined as the root mean square distance of atoms from the molecule's center of mass. Changes in (Rg) near surfaces indicate molecular flattening or extension due to adsorption forces (Samant et al., 2023).

Recent studies show that Rg distributions reveal adsorption-induced flattening and conformational rearrangement of molecules near interfaces for instance, polymers shrink and flatten on nanoparticle surfaces as polymer particle interaction strength increases (Li et al., 2020) and chains become more compact at droplet interfaces in biomolecular condensates (Wang et al., 2023). For example, Molecular dynamics studies have demonstrated that polymer chains undergo adsorption-induced conformational rearrangements at droplet interfaces, where analysis of the radius of gyration reveals chain flattening and compaction compared to the bulk state (Wang et al., 2023). Such interfacial effects are not limited to synthetic polymers; investigations of monoclonal antibody fragments at oil–water interfaces further indicate that adsorption drives partial unfolding and domain reorientation, phenomena that can be tracked via time-resolved Rg as a measure of tertiary compactness (Saurabh et al., 2024).

Recent simulations of polymer brushes demonstrate that adsorption-induced modifications in the radius of gyration (Rg) are quantitatively linked to brush height and interfacial morphology—scale-theoretical treatments confirm that Rg variations co-determine brush thickness (Vorsmann et al., 2023). Moreover, free-energy models incorporating both elastic stretching and entropic penalties have shown that Rg governs entropic barriers, influencing adsorption propensity and mass transport through interfacial brush layers (Swain et al., 2025). Together, these findings underscore that Rg serves as a sensitive diagnostic for adsorption-driven conformational transitions governing brush morphology, transport properties, and interfacial behavior in polymer systems.

2.6.3 Orientation Order Parameter

The orientation order parameter is a measure used to quantify the alignment or ordering of molecular or atomic orientations within a system and provides information about the alignment of molecules or atoms with respect to a reference axis or direction (Saleman et al., 2017). In research, the orientation order parameter is often employed in studies involving S-L interfaces, where molecular orientations play a significant role in determining material properties and behaviour. For instance, molecular dynamics simulations of water/n-alkane interfaces demonstrate that n-alkane molecules exhibit long-range alignment persistence and distinct layered structures captured by the orientational order parameter S_Z highlighted, C-shaped conformations and dependencies on chain length at the interface (Wilemski et al., n.d.).

In another exemplary study, the orientational order parameter was used to analyse molecular orientation in underground gas water interfaces, revealing H_2S-induced ordering effects important for interfacial behaviour (Chang et al., 2024). Furthermore, investigations in vacuum-deposited organic films quantified orientation order parameters SSS (Second-rank order parameter for transition dipole orientation) and BSB-Cz (emissive material with horizontal alignment tendency) molecules, demonstrating how interfacial deposition leads to horizontal molecular orientation directly validated against experimental values (Ishihara and Kaji, 2025). Collectively, these recent works confirm that orientational order parameters sensitively measure adsorption-driven orientation alignment, making them highly relevant to the current thesis' focus on molecular ordering near solid–liquid interfaces.

2.6.4 Heat Flux at S-L Interfaces

Irving and Kirkwood in 1950 initially identified the heat flux vector in Molecular Dynamics (MD) simulations by adapting expressions under the assumption of a uniform

system and absence of macroscopic fluid flow (Irving and Kirkwood, 1950). The heat flux for this study in MD simulations is derived from potential functions as elucidated. Additionally, the MD simulation's heat flux in molecular dynamics simulations is derived from many- body potentials and can be computed efficiently, ensuring conservation laws are met, and that algorithms have been developed to handle complex materials and scale linearly with system size, as demonstrated by (Boone et al., 2019; Torii et al., 2010).

Contemporary research has extended this to complex many-body potentials and interfacial systems, ensuring both algorithmic efficiency and physical accuracy. For example, recent work on machine-learning interatomic potentials introduces a heat-flux formulation that scales linearly with system size and is independent of many-body potential order, enabling efficient thermal conductivity calculations without compromising conservation laws (Langer et al., 2023). Corrections to LAMMPS implementations now properly account for three- and four-body interactions, rectifying errors of up to 100% in heat-flux estimates in earlier simulations (Boone et al., 2019). At solid–liquid interfaces, non-equilibrium MD simulations show how interfacial thermal conductance depends critically on surface properties functionalizing silica surfaces with hydroxyl groups can enhance interfacial heat transfer by up to eightfold, driven by molecular reorientation and adhesion energy changes (Mandrolko et al., 2025).

Similarly, recent MD studies elucidate how the presence of a liquid meniscus modifies spectral components of heat flux, linking vibrational mode coupling to wettability-dependent thermal conductance at the interface (El-Rifai et al., 2024b). These advanced implementations and interface-specific findings demonstrate how robust, modern heat-flux formulations grounded in Irving-Kirkwood fundamentals but extended to many-body potentials and interfacial complexities enable precise, scalable MD studies of thermal transport. This context underscores why your thesis can confidently adopt such formulations

to investigate heat flux at solid–liquid interfaces.

2.6.5 Interfacial Thermal Resistance

Interfacial thermal resistance, also referred to as Kapitza Resistance, quantifies the heat resistance experienced at S-L interfaces, leading to temperature discontinuities or drops at these interfaces (Hadjiconstantinou and Swisher, 2022). This resistance can be analysed in two parts, namely thermal boundary resistance (TBR).

While interfacial thermal resistance has been extensively studied, particularly in terms of thermal boundary resistance (TBR), limited studies have examined how this resistance behaves in molecular systems involving hydrocarbons C_4H_{10} and C_5H_{12} at S-L interfaces with varying FCC surface orientations. Furthermore, the interplay between molecular chain length and surface structure in governing temperature discontinuities remains inadequately understood at the atomic scale.

2.6.6 Thermal Boundary Resistance (TBR)

Thermal Boundary Resistance (TBR), also known as Kapitza resistance, quantifies the resistance to heat flow across the S-L interface. Recent papers have used non-equilibrium MD to study how polymer chain length and surface roughness jointly influence interfacial thermal resistance. They found that longer chains tend to align parallel to the interface reducing perpendicular heat transfer and that grooved surfaces increase resistance at low solid–liquid affinity while decreasing it when affinity is high. This tradeoff mirrors the sensitivity you're investigating with alkane chain length and FCC orientation (Luo et al., 2024b). Another study demonstrated how nearby interfaces (multiple layers) can significantly modify TBR, showing that TBR is not solely an intrinsic interface property but is also shaped by the local environment important when considering structured FCC surfaces

or adsorbed alkane layers (Adnan and Feng, 2024). Lastly, a 2023 chapter review by Ramos-Alvarado underscores that interfacial liquid density and layering contribute heavily to interfacial thermal conductivity; increased density at the interface raises conductance, thereby altering TBR a concept that complements your investigation into how alkane chain length modulates layering and contact (Ramos-Alvarado et al., 2024).

Together, these findings provide a strong foundation for your study, supporting why the interplay between alkane chain length, FCC surface orientation, and interfacial layering deserves focused investigation in your thesis. (Anandakrishnan and Sathian, 2023) Thermal Boundary Conductance (TBC), the reciprocal of TBR, quantifies heat transfer efficiency across solid–liquid interfaces. Recent research has demonstrated an exponential-to-linear crossover in TBC at Lennard–Jones solid–liquid interfaces as the solid–liquid interaction strength increased. This behaviour stems from interfacial solidification of the liquid and can be resolved using spectral heat-flux decomposition highlighting the dual roles of the interface and adjacent interfacial liquid region in determining thermal conductance (El-Rifai et al., 2024a). Another study revealed that TBC is not a purely local property; in Si/Ge interfaces, the presence of a neighboring interface can significantly enhance TBC sometimes from ~400 to ~700 MW/m²·K via phonon filtering effects (Adnan and Feng, 2024).

Furthermore, investigated solid–liquid (silica–water) interfaces and found that surface functionalization (e.g., replacing methyl groups with hydroxyl groups) can boost interfacial heat conduction by up to eightfold. This enhancement is attributed to increased adhesion energy, water molecule orientation realignment, and reduced depletion layers (Mandrolko et al., 2025). These insights collectively underscore how TBC depends not just on intrinsic material properties but also on interfacial chemistry, molecular ordering, and nearby environmental structure which aligns directly with your focus on how alkane chain length and FCC surface orientation affect thermal transport across interfaces.

Despite the growing use of MD simulations in evaluating interfacial thermal behaviour, several knowledge gaps remain. First, the influence of specific FCC surface orientations on thermal boundary resistance (TBR) and molecular adsorption in S-L interfaces has not been systematically analysed. Second, most prior works focus on either structural or thermal metrics in isolation, leaving a gap in integrated studies that correlate density, radius of gyration, and orientation order parameter with heat flux and TBR. Moreover, few studies consider the directional decomposition of heat flux or apply orientation order parameter to liquid alkanes near solid surfaces. Finally, the behaviour of liquid hydrocarbons like C_4H_{10} and C_5H_{12} in contact with gold surfaces remains underexplored in accessible MD studies.

2.7 Research Gap and Importance of Current Work

Despite the progress in MD simulations of S-L interfaces, significant gaps remain in lack of comprehensive studies combining FCC surface orientation with hydrocarbon chain length variations, limited data on molecular orientation and adsorption behaviour specific to FCC (100), (110), and (111) surfaces. And need for detailed analysis of interfacial thermal transport in systems beyond Lennard-Jones fluids, focusing on real alkanes like (C_4H_{10}) and (C_5H_{12}). This thesis addresses these gaps by systematically studying the combined effects of FCC crystal plane orientation and alkane chain length on heat transfer, adsorption, and molecular alignment using MD simulations. The findings will contribute to improved designs of nanoscale heat management systems and advanced lubrication technologies.

CHAPTER 3

METHODOLOGY

3.1 Introduction

This chapter provides an explanation of the simulation model, potential function, simulation algorithm, simulation method, method of validation, structural analysis of the density, orientation order parameter and radius of gyrations. Finally, the explanation regarding the heat flux calculations and measurements. It aims to investigate the adsorption mechanisms and heat transfer characteristic of different liquid hydrocarbons contacting solid surfaces through molecular dynamics simulations. The outline of this chapter is as follows:

- In Section 3.2 the details regarding the simulation model will be elaborated which consisted simulation size, and number of molecules utilised in the simulations
- In Section 3.3, the potential function utilised for the solid and liquid will be elaborated. The related equation will be given here.
- In Section 3.4, the details regarding the suitable algorithm utilised to calculate the position and velocity of each molecule.
- In Section 3.5 The details of the step for the simulation system utilised is explain here.
- In Section 3.6, the data analyses of the adsorption mechanism that consisted of the density, orientational order parameter and radius of gyration is elaborated. And finally in Section 3.7, the heat transport measurement and data evaluation is explained.

3.2 Simulation Model

The simulation model of S-L-solid layers is shown in Figure 3.1. The simulation model consists of liquid being placed between the two parallel solid walls of gold. The solid wall is structured as the Face-centered cubic (FCC) of gold (Au) of (100), (110), and (111). Butane (C_4H_{10}) and pentane (C_5H_{12}) of alkane group liquids are utilised in the simulation system, where each of the solid walls of FCC will be paired with each of the C_4H_{10} and C_5H_{12} alkane liquids in the simulation. Thus, there will be 6 simulation models for all of the FCC contacting the alkane liquids. In the simulation model, the molecules of C_4H_{10} and C_5H_{12} are guaranteed sufficient space to move and interact with one another by the distance of 60 Å as shown in Figure 3.1. The contact surfaces of solid and the liquid are referred to here as the S-L (S-L) interfaces, thus in each simulation model there are two S-L interfaces on the left and right sides of the simulation system.

The simulation model is a 3-dimensional box where the length in each direction is represented in terms of $L_x \times L_y \times L_z$ for the directions of -*x*, -*y*, and -*z*. The detailed size of the simulation box is shown in Table 3.1 along with the number of solid atoms arranged according to its lattice or structure of FCC in the directions of -*x*, -*y* and -*z*. The number of solid atoms presented in Table 3.1 shows only one side of the simulation system. In the simulation system, the number of solid atoms for each side of solid walls will have the same value for right and left sides. The simulation size for each of the FCCs is set separately to ensure that the size of the simulation system is approximately similar. Here, the distance in L_z, where the liquid is placed is selected in such a way that the solid wall interaction did not interfere at the center of the simulation systems.

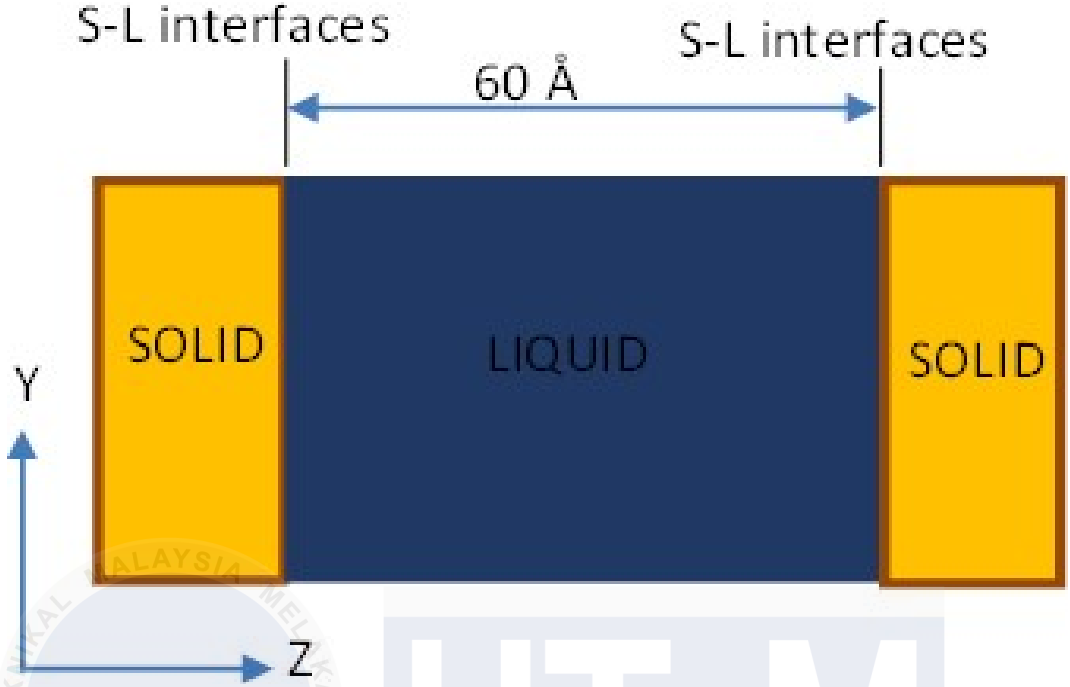

Figure 3.1 Liquid sandwiched in between two parallel solid walls

The number of liquid molecules of C_4H_{10} and C_5H_{12} are represented in Table 3.1. The number is identified through repeating trial and error. Then, the result of the liquid alkanes density is compared to the density of saturated liquid of C_4H_{10} and C_5H_{12} at 70 percent from the critical temperature (T_c) of the liquid. This is the only way of making sure that the molecules of C_4H_{10} and C_5H_{12} behave in similar conditions to real liquid.

Table 3.1 The size of the simulation box and number of solid atoms based on the types of crystal planes

Liquid Alkane	Types of FCC crystal planes	Size of simulation box $L_x \times L_y \times L_z$ (Å^3)	Number of solid atoms in x, y, and z-axes
Butane (C_4H_{10})	100	40.729 × 40.729 × 114.437	10 × 20 × 6
	110	46.080 × 48.875 × 118.800	16 × 12 × 10
	111	40.320 × 39.906 × 118.218	14 × 16 × 6
Pentane (C_5H_{12})	100	40.729 × 40.729 × 114.437	10 × 20 × 6
	110	46.080 × 48.875 × 118.800	16 × 12 × 10
	111	40.320 × 39.906 × 118.218	14 × 16 × 6

Table 3.2 The number of molecules for liquid alkane based on the three types of crystal plane (100), (110), and (111)

Liquid Alkane	Types of FCC crystal planes	Number of molecules for liquid alkane
Butane (C_4H_{10})	100	503
	110	683
	111	491
Pentane (C_5H_{12})	100	445
	110	586
	111	433

3.3 Interaction Forces

3.3.1 Liquid Model

The simulation model uses the united atom (UA) model of the NERD potentials for representing the linear alkane liquid consisting of C_4H_{10} and C_5H_{12}. In previous studies (Samant et al., 2023; Xia et al., 2023) have been utilised similar model and found out that the results are closely replicated real liquid with optimum computation time, thus an identical contact forces were employed for these simulations. In the UA NERD the interactions are replicated by three bonded interactions, namely bond bending, bond stretching, and torsion. On the other hand, there are also non-bonded interactions, which is the Van der Waals interaction. The bonded interaction and non-bonded interaction can be self-explained in Figure 3.2.

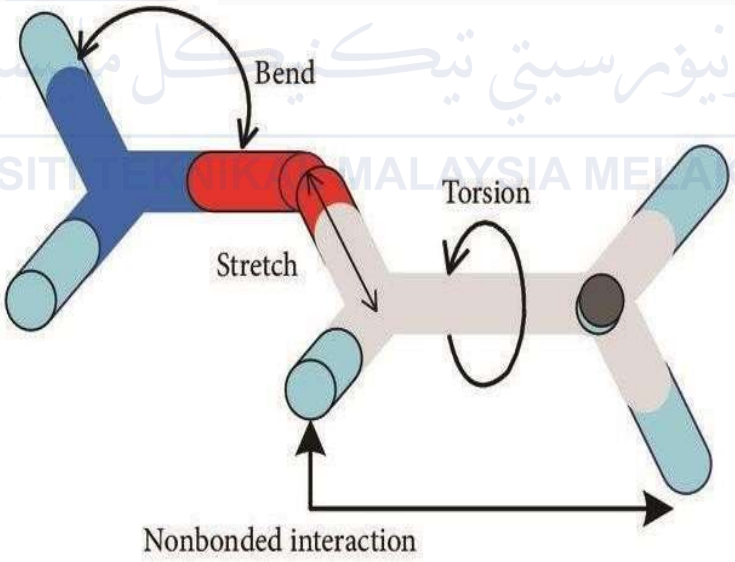

Figure 3.2 AU NERD force equation for force field bonded and non-bonded interactions (Iqbal et al., 2018)

3.3.2 Bonded Interactions

In the UA NERD, the hydrogen atom is grouped in a single interaction site located as carbon atom, thus in the alkanes liquid it consists of CH_3 and CH_2 pseudoatoms. These pseudoatoms connected to each other creates a linear chain of liquid alkanes. For C_4H_{10},

there are two CH_3 pseudoatoms and two CH_2 pseudoatoms, whereas for C_5H_{12}, there are two CH_3 pseudoatom and three CH_2 pseudoatoms at the center of the molecules.

The bonded interaction which is mentioned earlier comes from 3 interactions which are bond stretching, bond bending and torsion interaction forces. The bond stretching refers to the changes in distance between two bonded atoms within the molecules. As these molecules interact with the solid surface, the stretching of bonds occurs due to thermal fluctuations (Math et al., 2022). The potential functions are given as following:

$$U(r_{ij}) = \frac{k_r}{2} \left(r_{ij-} b_{eq}\right)^2 \tag{3.1}$$

Where k_r is 1.3323 x 10^{-18} J/Å^2 and be_{eq} is 1.54 Å. The second interaction is bond bending which involves changes in the angles between bonds within the alkane molecules. This can be significant to determine how these molecules orient and behave at the interface with the solid surfaces. Bond bending occurs between adjacent atoms within a molecule and is represented by the harmonic potential, which is defined as follows: (Saleman et al., 2019).

$$U(\theta) = \frac{k_\theta}{2} (\theta - \theta_0)^2 \tag{3.2}$$

Where k_θ = 8.6291 x 10^{-19} J/rad^2, and θ_0 = 114.0°. And finally, torsion refers to the twisting or rotational deformation of a molecule under the influence of a torque or twisting force. Molecular dynamics simulations involve the rotational movement of the molecular segments of alkanes along their bond axes. Understanding the rotating motion is

essential for comprehending the many shapes that alkane chains adopt when they are in contact with S-L interfaces, as well as how they interact with solid surfaces (Math et al., 2022). The torsion potential arises between any four nearby atoms in a molecule and is defined as follows:

$$U(\varphi) = V_0 + V_1\,(1 + \cos\varphi) + V_2\,(1 - \cos 2\varphi) + V_3(1 + \cos 3\varphi \quad (3.3)$$

Where φ is the dihedral angle, and V_0 =0 J, V_1 = 4.9018 x 10^{-21}J, V_2 =-9.4146x10^{-22}J and V_3 = 1.0925x10^{-20}J.

3.3.3 Non-bonded interactions

Studies encompass forces that act between atoms or molecules that are not chemically bonded to each other. These forces are critical in determining how the alkanes adsorb onto and move across the solid surfaces, influencing the overall behaviour of the S-L interface, The nonbonded interaction is treated by Lennard Jones (LJ) 12-6 potential which is given as follows. (Math et al., 2022; Naga Parameswara Gupta, 2022).

$$U^{Lj}(r_{ij}) = 4\varepsilon_{ij}\left[\left(\frac{\sigma_{ij}}{r_{ij}}\right)^{12} - \left(\frac{\sigma_{ij}}{r_{ij}}\right)^{6}\right] \quad (3.4)$$

where r_{ij} is the distance between atoms i and j. The energy parameters are ε is 2.0433 × $10^{-21}\,J$ and the size parameter for LJ potential, σ is 3.73 Å (Saleman et al., 2019, 2017) The Lennard-Jones (LJ) potential, which delineates the interaction between atoms or molecules, was initially discovered by John Edward Lennard-Jones. Previous studies have extensively used the LJ potential to characterise the features of liquids in respect to thermal energy (Estrada, 2004; Wang et al., 2020). The LJ potential model can be divided into two

components: a steep repulsive term and a gentler attractive term, which represent dispersion forces. The 12-6 Lennard-Jones potential model is a prevalent representation of the LJ potential, which is frequently employed in numerous force fields.

3.3.4 Solid Model

The Morse potential, which was discovered and named by Philip M. Morse in 1929, is frequently used to simulate atomic systems (Aldossary, 2021; Aldossary and Al Rsheed, 2020; Peña et al., 2021). Morse potential was employed to model the solid walls, as they effectively and accurately capture the atomic behaviour. The morse potential can be represented using the following mathematical model as:

$$\Phi(\mathrm{r_{ij}}) = D[e^{-2\alpha(r_{ij}-r_0)} - 2e^{-\alpha(r_{ij}-r_0)}] \tag{3.5}$$

The above equation represents the interaction distance, r_{ij} , between two atoms i and j. The coefficient D is 7.6148 × 10^{-13} erg, equilibrium between two atoms, r_0 is 3.0242 Å and α is 1.5830 Å $^{-1}$. In this simulation, the gold atom is considered as the electrically insulating material where heat conduction through free electrons is neglected in the calculations.

3.3.5 Solid to Liquid Interactions

TheThe simulation employs the combined principles of Lorentz–Berthelot, originally developed by Hendrik A. Lorentz and Daniel Berthelot. These principles are used to mimic the forces that interact between solids and liquids, and such identical interactions and forces have been widely employed in previous research studies (H. Wu et al., 2023; Yu et al., 2023). The Lorentz combining rule for the Lennard–Jones size parameter is expressed as:

$$\sigma_{ij} = \frac{\sigma_{ii} + \sigma_{jj}}{2} \tag{3.6}$$

where σ_{ii} and σ_{jj} are the size parameters of species iii and jjj. This equation represents the arithmetic mean of the size parameters. The Berthelot combining rule for the Lennard–Jones energy parameter is given by:

$$\epsilon_{ij} = \sqrt{\epsilon_{ii}\epsilon_{jj}} \tag{3.7}$$

where ϵ_{ii} and ϵ_{jj} are the energy parameters of species ii and jj. The equation averages these parameters geometrically, reflecting isotropic behaviour in stress distribution, especially in multi-phase interactions like solid–liquid interfaces.

3.4 Reversible Reference System Propagator Algorithm (r-RESPA)

The Reversible Reference System Propagator (r-RESPA) Algorithm is a critical time-stepping method utilised in molecular dynamics (MD) simulations to effectively advance the system's state over time. Initially, it distinguishes between short-range and long-range forces, considering the former as reference system forces and precisely calculating the velocities for the final. This distinction enables more rapid simulations, which is especially advantageous for larger systems that necessitate extensive computation (Abreu and Tuckerman, 2021; Martin et al., 2025; Shaw et al., 2010). In the present simulations the r-RESPA is utilised for the time integrations, where 1 femto second (fs) and 0.2 fs is utilised for the intramolecular motions and intermolecular motion respectively.

3.5 Simulation Method

Initially, the simulation system was run at 0 Kelvin (K) over a period of 1 to 200,000 time steps for molecular relaxation. Next, the temperature of the system is slowly raised to

0.7 T_c (critical temperature) of the C_4H_{10} and C_5H_{12} liquids for 2 to 500,000 times step. The velocity scaling methods are used to regulate the temperature of the simulation system (Rauscher et al., 2022). Subsequently, the simulation system was regulated and sustained at a consistent temperature of 0.7 T_c of the linear liquid alkane over a duration of 1 to 2 million time steps.

Then, a temperature difference was set to the simulation system where a high temperature is set on the left side, and a low temperature was set on the right side of the simulation system. The setup was run for 2 to 3 million timestep. Finally, the data acquisition were collected for heat flux, position, and velocity data, covering at range of 10 million timestep. The variation in the time step is due to the convergence characteristics that appear in each of the simulation systems. Larger or longer time steps show that the simulation system required more time steps to be converged.

3.6 Structural Quantities Measurement

3.6.1 Density Distributions and validations of simulation model.

Measuring density distributions is crucial for validating the presence and behaviour of the liquid trapped between solid walls. The density profile of the liquid near the S-L interfaces will be analysed to understand the adsorption mechanisms and interactions (Lin et al., 2022). Density Distributions of the liquid alkanes confined between the two solid walls were calculated by dividing the simulation system into 2400 with the thickness of approximately 0.05 Å in the z- direction.

In order to validate the model in this simulation system, the density distribution in the present study is compared to the past system at the constant temperature. Figure 3.3 shows the density distribution of C_4H_{10} and C_5H_{12} liquid. The purple and vertical dashed lines represent the S-L interfaces. The flat distribution that developed at the center of the simulation is referred to here as the bulk-like region.

In Figure 3.3, the flat distribution is measured in order to obtain the similar value of the saturated liquid density at 0.7 T_c. The orange, yellow, and green line is indicated as density distribution of C_5H_{12} and indigo, grey, blue line represent C_4H_{10} for three different crystal planes of FCC (100), (110), and (111). From previous investigation it is found that the critical T_c for C_5H_{12} is 469.70 K and the density at the 0.7 T_c is 590 kg/m^3 (Saleman et al., 2019) and the T_c for C_4H_{10} is 436.2 K and the density at the 0.7 Tc is 540 kg/m^3(Saleman et al., 2017). Based on Figure 3.3 it is understood that at the bulk-like region the average value of density for C_4H_{10} is approximately at 540 kg/m^3 and for C_5H_{12} is approximately at 590 kg/m^3, thus the simulation model is validated.

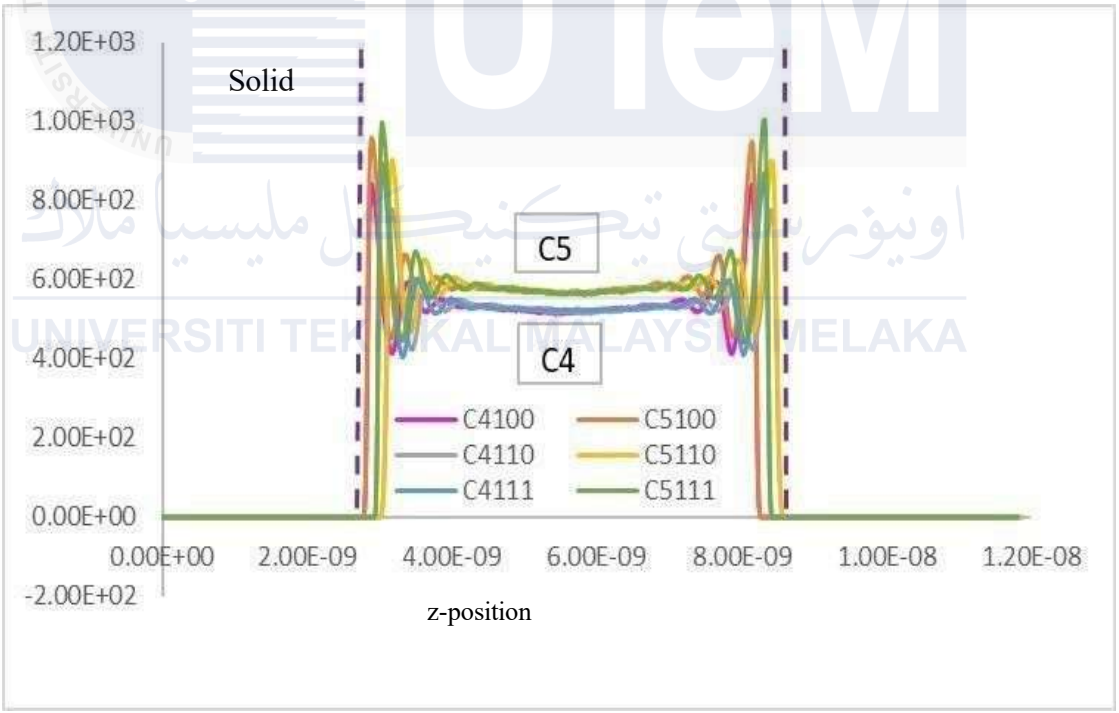

Figure 3.3 Density distribution of C_4H_{10} and C_5H_{12} liquids for FCC (100), (110), and (111) crystal plane

3.6.2 Radius of Gyration

Radius gyration is a method to determine the shape and orientation of liquid molecules in relation to the solid surfaces (Dong et al., 2022; Zhan et al., 2019). This parameter helps in validating the molecular arrangements and adsorption behaviours at the

S-L interfaces by using equation below:

$$R^2 = \frac{1}{N}\left\langle \sum_{i=1}^{N} (r_i - r_{cp})^2 \right\rangle \tag{3.8}$$

The value of R^2 corresponds to the square of the radius of gyration. The utilization of the square in this context is mostly for mathematical expediency and to guarantee the maintenance of consistent units. The radius of gyration (R) is equal to the square root of R^2. N represents the aggregate quantity of particles, including atoms and molecules, within the system. The formula calculates the mean of the squared distances of all particles in order to represent the overall distribution. The $\langle\ \rangle$ angle brackets represent the average value of a set of variables. In a dynamic system, such as molecules undergoing thermal motion, the spatial coordinates of the particles undergo temporal variations. The ensemble average encompasses the calculation of the average across all conceivable configurations of the system, which can also be regarded as a temporal average. The notation $\sum_{i=1}^{N}$ represents the summation operation, which involves adding together the individual contributions of all N particles in the system.

The symbol r_i represents the location vector of the particle within the system. It denotes the magnitude and direction of the displacement of this particle from a selected reference point. The symbol r_{cp} represents the position vector of the center of mass of the system. The center of mass is a singular point that symbolizes the mean location of all the mass inside the system. The geometric center can also be considered for homogeneous density. The expression $\sum\ (r_i - r_{cp})^2$, calculates the squared distance between each particle and the center of mass. By squaring the distance, we guarantee that all values are positive and give more importance to particles that are located at a greater distance. This equation calculates the root mean square distance of each atom or particle from the center of mass,

which gives a quantitative estimate of the overall size and shape of the molecular system. Practically, the computation entails finding the centroid and the distances of specific atoms or particles from it.

3.6.3 Orientation Order Parameter

Evaluating the orientation order parameter to determine the positioning of liquid molecules (parallel, perpendicular, or random) near the solid surfaces. The orientation order parameter is frequently utilised in research to investigate S-L interfaces, where molecule orientations have a substantial impact on material properties and behaviour (Rao et al., 2015; Zeng et al., 2022). A common method for quantifying the orientation order parameter is by using calculations that include spherical harmonics or tensorial representations of molecular orientations, as expressed below:

$$S = \frac{1}{2}\langle 3\,cos^2\,\theta - 1\rangle \tag{3.9}$$

The orientation order parameter, denoted as S, ranges from -0.5 to 1. A value of 1 signifies perfect alignment along the reference axis, 0 signifies random orientation, and -0.5 signifies perfect alignment perpendicular to the reference axis. The angle brackets ⟨⟩ denote the mean value calculated over all molecular segments or molecules under consideration in the system. The process of averaging can occur either over a duration of time for an individual molecule or over a group of molecules at a specific moment in time. The phrase $\langle cos^2\theta\rangle$ represents the square of the cosine of the angle θ, which is the angle between the axis of a molecule and the reference direction. The square of the cosine function accentuates the alignment by amplifying the function's value at acute angles.

The orientation order parameter is highly valuable in the investigation of C_4H_{10} and C_5H_{12} liquid crystals, as it determines the optical and mechanical characteristics of the

material based on the extent of molecular alignment. These computations enable researchers to evaluate the alignment of molecules inside the system.

3.7 Measurement of Heat Flux

In their initial work in 1950, Irving and Kirkwood found the heat flux vector in Molecular Dynamics (MD) simulations by modifying formulas based on the assumption of a uniform system and the absence of macroscopic fluid movement (Irving and Kirkwood, 1950). The heat flux in this study is calculated using potential functions, as explained. In molecular dynamics simulations, the heat flux is calculated using many-body potentials. This calculation is efficient and ensures that conservation laws are obeyed. Furthermore, algorithms have been developed to handle complex materials and scale linearly with the size of the system, as demonstrated by (Boone et al., 2019; Rafeq Saleman et al., 2022). The heat flux, represented by the symbol J, is calculated by multiplying the control volume, designated as V, as shown in Equation (3.10):

$$J_x V = J_x V = \sum_{x}^{N} v_{x,s} E_s + \sum_{n-body\ potential} \sum_{s_1} \sum_{s_2 > s_1} \cdots \sum_{s_n > s_{n-1}} \left[\frac{1}{n} \sum_{\alpha=1}^{n-1} \sum_{\beta=\alpha+1}^{n} (F_{s_\alpha,u} . V_{s_\alpha} - F_{s_\alpha,u} . V_{s_\beta})(x_{s_\alpha} - x_{s_\beta}) \right] \tag{3.10}$$

$$J_x V = J_x V = \sum_{x}^{N} v_{x,s} E_s + \sum_{n-b} \sum_{potential} \sum_{s_1} \sum_{s_2 > s_1} \cdots \sum_{s_n > s_{n-1}} \left[\frac{1}{n} \sum_{\alpha=1}^{n-1} \sum_{\beta=\alpha+1}^{n} (F_{s_\alpha,u} . V_{s_\alpha} - F_{s_\alpha,u} . V_{s_\beta})(x_{s_\alpha} - x_{s_\beta}) \right] \tag{3.11}$$

$v_{x,s}$ represents the velocity in the x-direction of site s, E_s denotes the internal energy of sites.

V_{s_α} indicates the velocity vector. $F_{s_\alpha,u}$ depicts the force acting on site S. $(x_{s_\alpha} - x_{s_\beta})$ explains the distance in the X-direction between $s_\alpha$and s_β within the control volume, V.

3.7.1 Interfacial Thermal Resistance

Interfacial thermal resistance, known as Kapitza Resistance, measures the resistance to heat transfer at interfaces between solids and liquids. This resistance causes temperature discontinuities or decreases at these interfaces (Dong et al., 2024; Mohammadian et al., 2024). Comparing temperature differences to heat flux at S-L interfaces to determine interfacial thermal resistance, which reveals the relationship between heat transport and adsorption behaviour. In normal cases the interfacial thermal resistance is evaluated by thermal boundary resistance (TBR).

Thermal Boundary Resistance (TBR) is a measurement used to evaluate the resistance to heat transfer at the interfaces of solids and liquids on a molecular level (Deng et al., 2019). The definition of TBR is based on the ratio of the temperature jump (TJ) across the S-L interface over the heat flow *Jx* passing through, as represented by the following equation:

$$TBR = \frac{TJ}{J_x} \tag{3.12}$$

The formation of a thermal boundary resistance (TBR) is influenced by the heat flux at two separate surfaces, resulting in the creation of a thermal junction (TJ) (Kurzawski and Ezekoye, 2020). The management of TBR at the S-L (S-L) interfaces is determined by the interaction of molecules. TBR can also be influenced by the molecular-scale structure of two distinct interfaces in contact (Issa and Mohamad, 2012).

3.8 Summary

This thesis investigates the adsorption mechanisms of liquid hydrocarbons on solid surfaces and the associated thermal transport phenomena at S-L interfaces using molecular dynamics (MD) simulations. The study focuses on the interactions between butane (C_4H_{10}) and pentane (C_5H_{12}) liquids and gold (Au) surfaces represented by face- centered cubic (FCC) planes (100, 110, 111).

Key contributions include the development of a simulation model employing the united atom (UA) approach and NERD potential functions to capture the interactions and structural properties at the interface. Advanced algorithms like r-RESPA were used to enhance computational efficiency and precision. Measurements of density distributions, orientation order parameters, and radius of gyration provide insights into the structural and dynamic behaviour of molecules.

Finally, the thesis also explores thermal boundary resistance (TBR) and thermal conductivity at the interfaces to understand heat transport mechanisms. By analyzing factors such as interfacial thermal resistance, adsorption behaviour, and molecular alignment, this research contributes to optimizing materials for applications in thermal management and material science.

CHAPTER 4

RESULTS AND DISCUSSION

4.1 Introduction

This chapter presents the results of the S-L interfaces of the simulation system. In the first part the results of the structural quantities of density distribution, orientation order parameters, and radius of gyration will be discussed. In the second part the results of the heat flux, temperature distributions, and thermal boundary resistance will be discussed.

4.2 The analysis of Structural Quantities

4.2.1 Density Distribution

Density refers to the measure of molecules of how much mass is contained in a given volume of a substance. The distribution of liquid alkanes, contained between two solid walls, was determined by partitioning the simulated system into slabs with a thickness of roughly 0.01 Å in the z-direction. The density of each slab was determined by counting the quantity of CH2 and CH3 in each slab. Figure 4.1 shows density distributions of butane (C_4H_{10}) liquid contacting FCC of (100) on both sides of the simulation systems. Based on the figure, A is the first adsorption layer, B is the second adsorption layer, and C is the third adsorption layer. The dotted black line signifies the S-L interface layer.

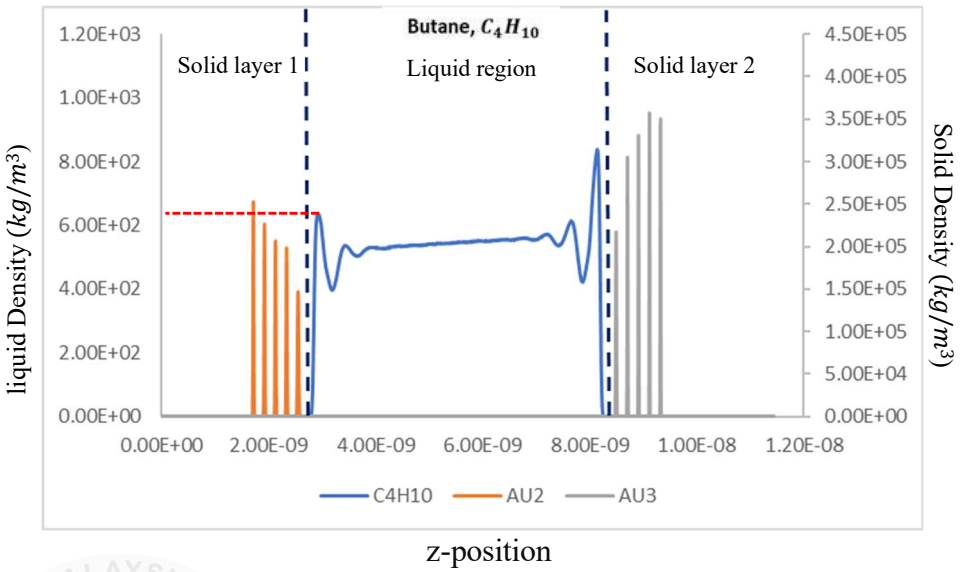

Figure 4.1 Density distribution of liquid butane (C4H10) confined between two Face-centered Cubic crystal plane of (100) on both sides of the simulation system

Based on Figure 4.1, the FCC crystal plane (100), the solid walls exhibit 5 layers of peaks that correspond to the layers of solid atoms arranged in a lattice arrangement (orange lines on left side and gray lines on left sides of the simulation system). Similar characteristics have been observed for other types of liquids and crystal planes. A significant different can only be observed for FCC (110) crystal plane, due to the facts that FCC (110) exhibit 9 layers of solid as provided in appendix. The similar characteristics were also observed by previous researcher (Chilukoti et al., 2013; Zhang et al., 2025).

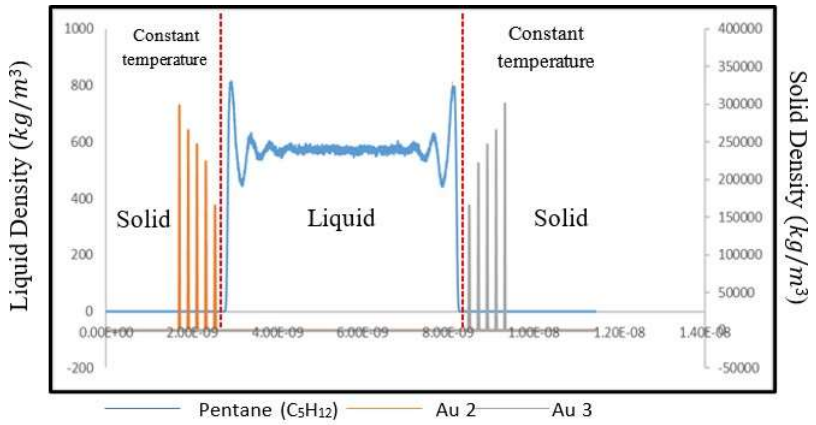

(a) FCC 100

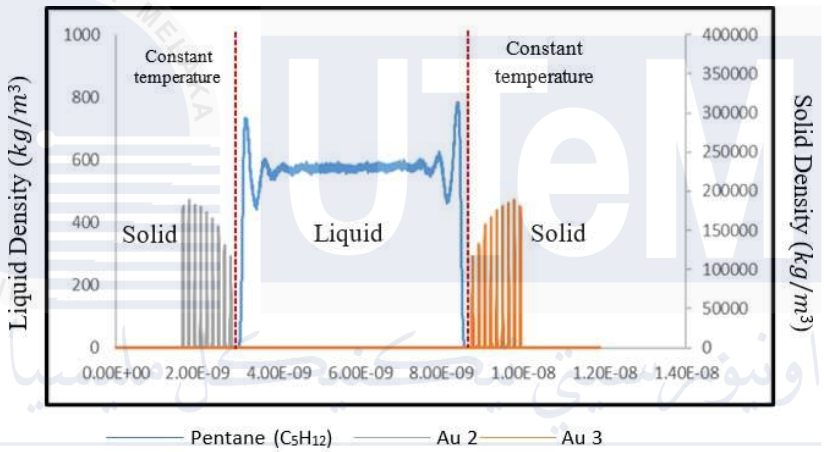

(b) FCC 110

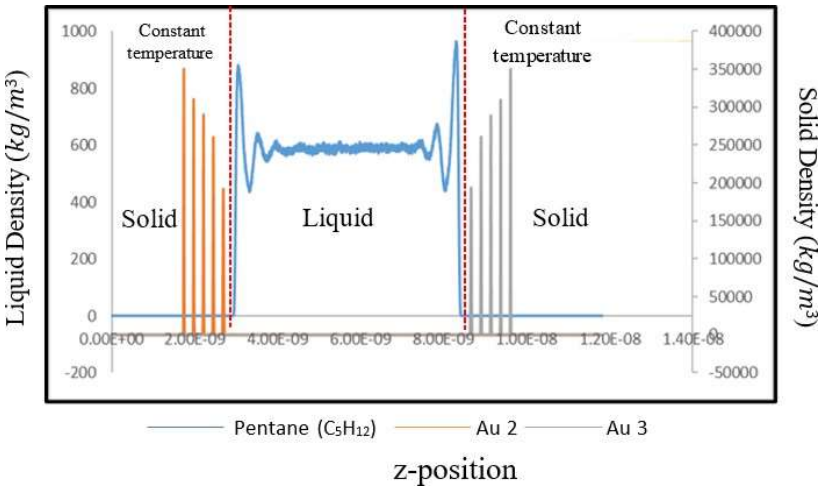

(c) FCC111

Figure 4.2 Comparison between C_5H_{12} crystal plane 100 (a), 110 (b), and 111 (c) at constant temperature

Figure 4.2 illustrates the density distribution for C_5H_{12} liquid in contact with (a) 100 , (b) 110, and (c) 111 crystal planes at constant temperature. As shown in Figure 4.2, five solid structure layers were used for the (100) and (111) crystal planes, while nine layers were used for the (110) plane. This configuration ensured that all simulation systems maintained a comparable size, regardless of the FCC structure. In the density profiles, the first adsorption layer near the solid-liquid interface for the (100) crystal plane exhibits a peak height of 801.786 kg/m^3. As shown in Table 3.1, the (110) crystal plane exhibits a slightly lower peak density of 784.756 kg/m³, while the (111) plane demonstrates the highest peak density at approximately 966.940 kg/m³. This difference is attributed to the variation in the number of atoms present in the simulation system for each crystal plane, where higher number of solid atom present near the S-L interface exhibit higher peak density. However, the density profiles for the solid layers across all three crystal planes show a consistent trend, with peak heights decreasing as they approach the S-L interface. This behaviour is attributed to stronger fluctuations of solid molecules at the interface. These observations align with findings from previous studies by (Chilukoti et al., 2013). As seen in Figure 4.2, the average peak height for the solid wall in (111) shows the highest value, followed by (100) and (110), which is expected since the number of molecules for each solid layer is different between FCCs, and (111) has the highest value and the highest number of molecules present in each solid layer.

The number of atom present in the first layer of FCC (100) is 200, FCC (110) is 192 and FCC (111) is 224. Regarding this setup, the adsorption layers for the liquid also experience the same trend, where the first peak of the liquid, which is located next to the S-L interfaces, has the highest peak height for (111), followed by (100) and (110). Although the simulation systems exhibit approximately similar system sizes, the adsorption behaviour of the liquid at the S-L interfaces is different. Although the number of molecules for FCC (110) has the largest number of molecules present in each bulk solid, the adsorption layers of liquid adjacent to the solid layer show the lowest peak height. Thus, according to the

results, the number of molecules in the liquid next to the liquid layer plays a significant role in determining the adsorption behaviour of the liquid at the solid surfaces, which relates to the attraction and retraction forces between the solid and liquid. Previous studies support this observation, where observed that Au(111) surfaces yield the highest first-layer liquid peak density, while Au(110) exhibits the lowest adsorption among the FCC planes. Their work links surface atomic density and lattice structure to interfacial liquid layering a trend that matches our data on C_5H_{12} behaviour across (100), (110), and (111) orientations (Saleman et al., 2017). It highlights how variations in surface structures, such as FCC orientations, influence liquid layering, peak density, and adsorption trends near solid surfaces.

Figure 4.3 illustrates the density distributions of C4H10 and C5H12 liquids in contact with (100), (110), and (111) crystal planes with high temperature (0.75 *Tc*) is set at the left sides and low temperature (0.65 *Tc*) is set on the right side of the simulation system. At lower temperatures, the adsorption layer of liquid near the S-L interface exhibits sharp peaks, indicating strong molecular packing. As the temperature increases, the peak height decreases, reflecting enhanced molecular movement and reduced adsorption strength. Similarly, C_5H_{12} displays the adsorption layers of liquid at lower temperatures, a distinct and sharp peak are observed near the interface, while at higher temperatures, the peaks become broader and less defined. This behaviour indicates a reduction in adsorption strength at higher temperatures.

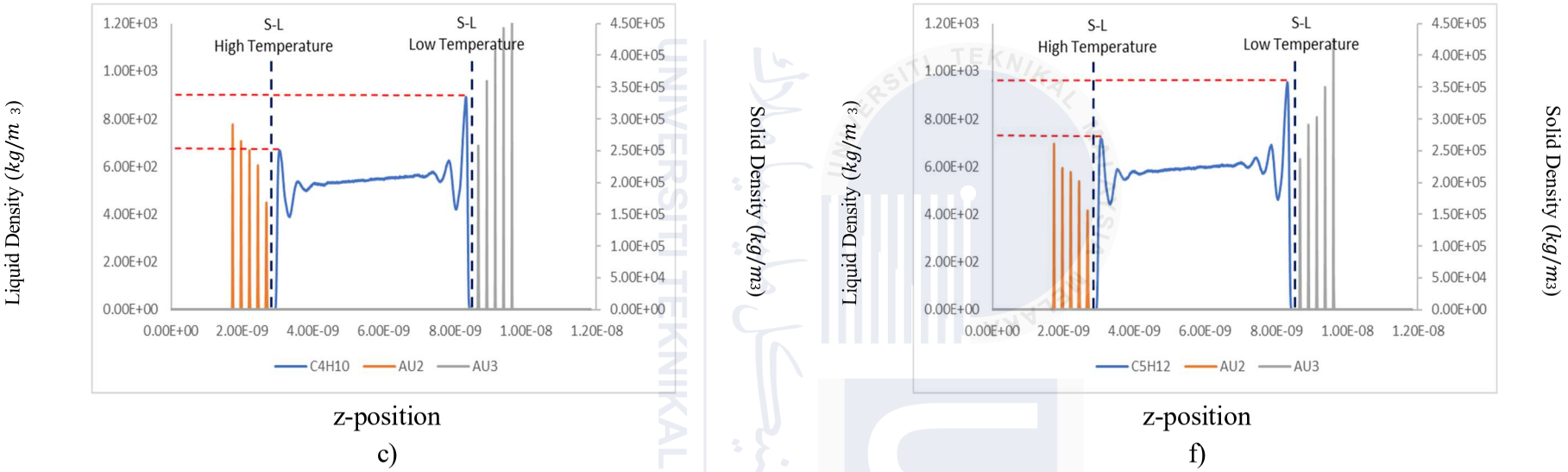

Figure 4.3 Density distribution of butane C_4H_{10} contacting crystal plane of (100) (a), (110) (b), (111) (c) and Pentane C_5H_{12} contacting crystal plane of (100) (d), (110) (e), and (111)

The density profile analysis reveals that temperature significantly impacts the adsorption behaviour and structural arrangement of C_4H_{10} and C_5H_{12} hydrocarbons at the S-L (S-L) interface. At lower temperatures, both hydrocarbons exhibit sharp and pronounced density peaks near the interface, indicating strong molecular packing and higher adsorption strength. As the temperature increases, these peaks become broader and less defined, reflecting enhanced molecular arrangement, weaker adsorption forces, and increased thermal fluctuations. C_5H_{12}, being a larger molecule, generally shows higher peak density values compared to C_4H_{10} at lower temperatures, highlighting its stronger adsorption capacity. However, both hydrocarbons follow a consistent trend of decreasing peak heights with rising temperatures. Additionally, slight asymmetry in peak values on the left and right interface regions suggests the influence of molecular arrangement and thermal motion.

Previous researchers examined how temperature affects adsorption and transport of n-alkane molecules at solid boundaries. They observed that lower temperatures produce sharp, well-defined adsorption layers, while higher temperatures result in broader, attenuated density peaks, indicating weaker adsorption and enhanced molecular motion. These results mirror our behaviour of C_4H_{10} and C_5H_{12} as temperature rises a larger molecule like pentane shows stronger adsorption at low temperatures but follows the same decreasing trend with temperature. The slight left–right asymmetry in peak heights further aligns with their findings on thermal fluctuation and molecular arrangement near interfaces (Hamal et al., 2021). These findings closely mirror our observations for C_4H_{10} and C_5H_{12} systems, thereby reinforcing the interpretation of the temperature-dependent adsorption trends described in our density profile analysis. It provides insights into the mechanisms of adsorption and the factors affecting interfacial interactions, which are relevant to understanding the adsorption behaviour of hydrocarbons at S-L interfaces.

4.2.2 Radius of Gyration

The radius of gyration is a structural property used to determine the shape of liquid molecules. It provides insights into the molecular shape and distribution that are reflected by adsorption behaviour of liquid hydrocarbons. The radius of gyration is analysed along the *x-* , *y-*, and *z-axes* to clarify the adsorption mechanism, which is aligned with the objective. The current work determines the mean square radius of gyration as the ensemble average of a slab, as established by (Chilukoti et al., 2013)

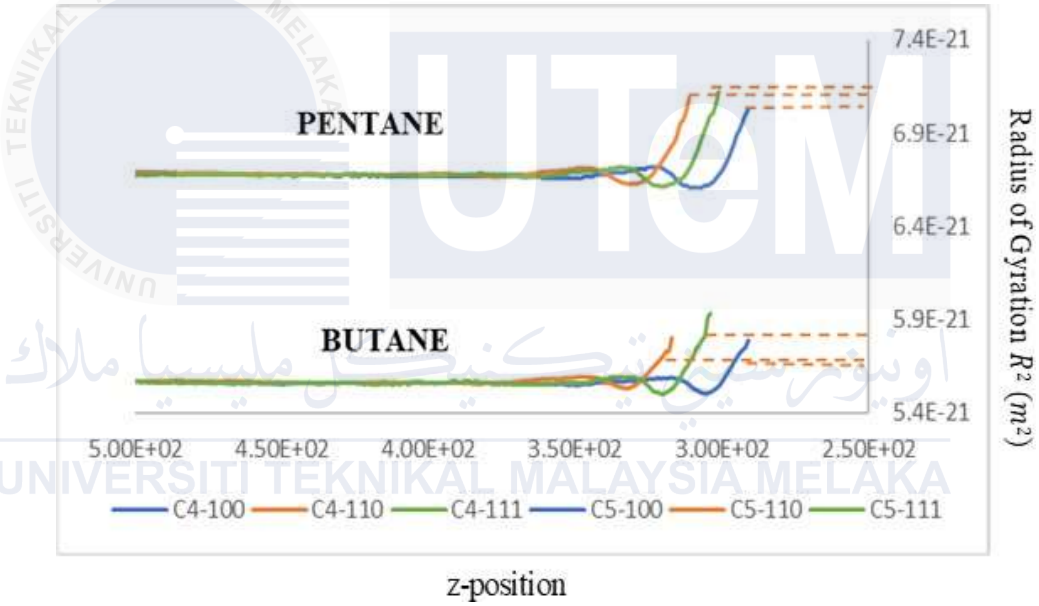

Figure 4.4 Overall Radius of gyration for C_4H_{10} and C_5H_{12} contacting the (100), (110), and (111) crystal planes

Figure 4.4 displays the radius of gyration profiles for the (100), (110), and (111) crystal planes facing C_4H_{10} and C_5H_{12} liquids. The comparison between liquid hydrocarbons, specifically C_4H_{10} and C_5H_{12}, across different FCC crystal planes (100), (110), and (111) reveals both similarities and differences in their behaviour and structural properties. Based on the results of the overall radius of gyrations it is understood that the value of radius of gyration for C_5H_{12} is higher than C_4H_{10} regardless the types of crystal planes. Near the S-L interfaces it is found that regardless the types of liquid the (100) crystal planes have the lowest value of radius gyration followed by (110) and (111). In addition, regardless the types

of crystal planes all FCC exhibits approximately similar value for the same liquid. These distinctions are primarily influenced by the molecular characteristics of each hydrocarbon and their interactions with the crystal plane surfaces. One of the key similarities between C_4H_{10} and C_5H_{12} lies in their adsorption patterns across the FCC planes. Both hydrocarbons exhibit structural organization influenced by the specific arrangement of atoms on each crystal plane (100), (110), and (111).

In order to further understand the characteristics of the liquid shape in the simulation system, the radius of gyrations is further divided in the direction of *-x, -y* and *-z*. In the next section further, explanation will be elaborated according to the divided direction and liquid hydrocarbon. The *-x* and *-y* axes of liquid shape shows that the liquid is oriented parallel to the solid surfaces and in the z- directions shows that the liquid shape in the normal direction to the solid surfaces. Notably, FCC planes exhibit similar radius of gyration values for the same hydrocarbon, signifying consistent adsorption patterns and structural organization. These findings highlight the interplay of molecular properties and crystal surface characteristics in determining hydrocarbon behaviour (Frenkel and Smit, 2023).

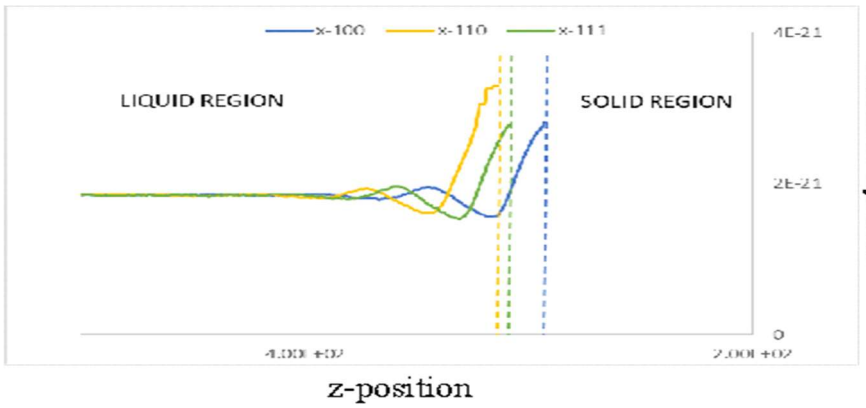

(a)

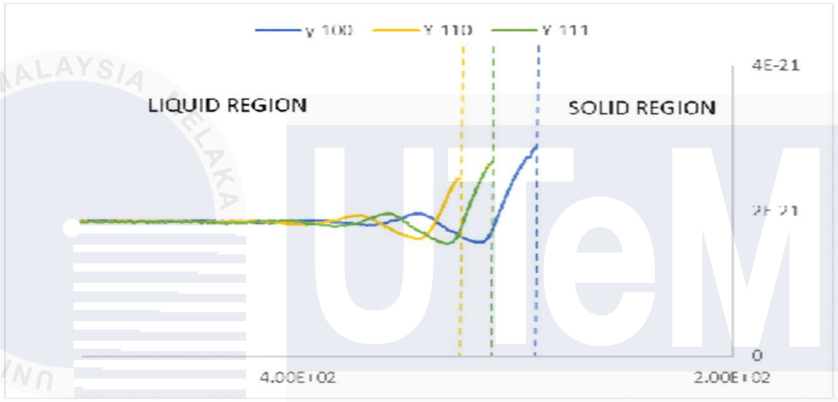

(b)

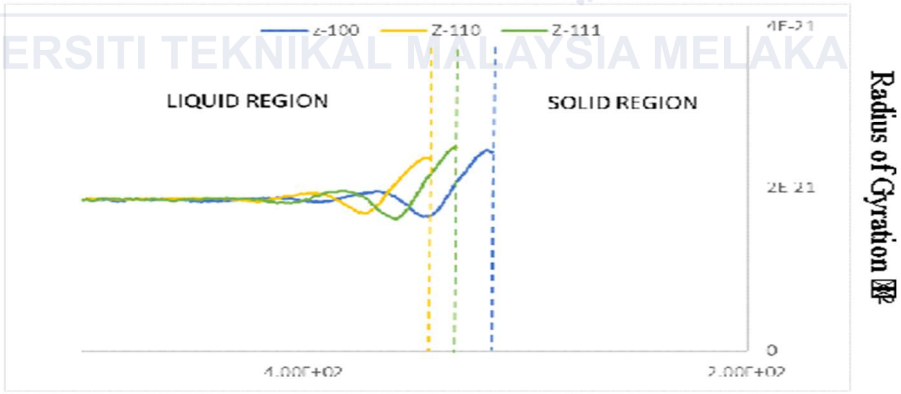

(c)

Figure 4.5 Radius of gyration on x-axes (a), y-axes (b), and z-axes (c) for butane C_4H_{10} contacting crystal plane of (100), (110), (111)

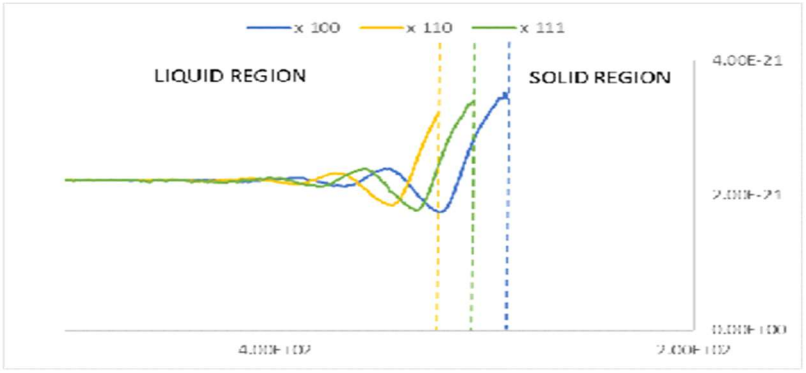

(a)

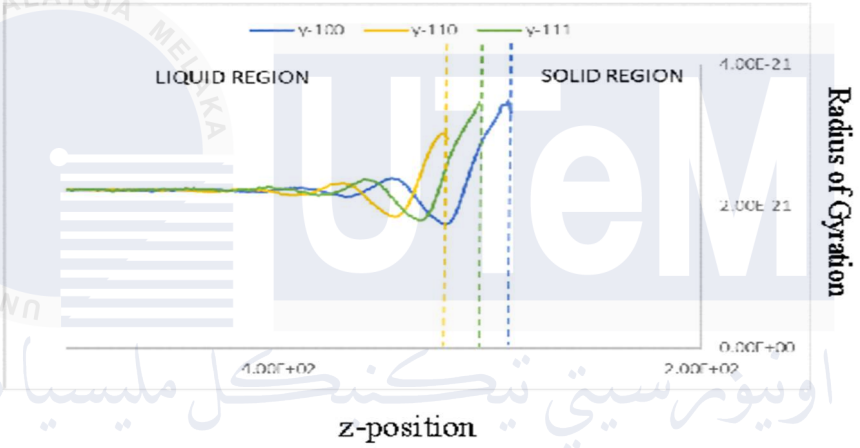

(b)

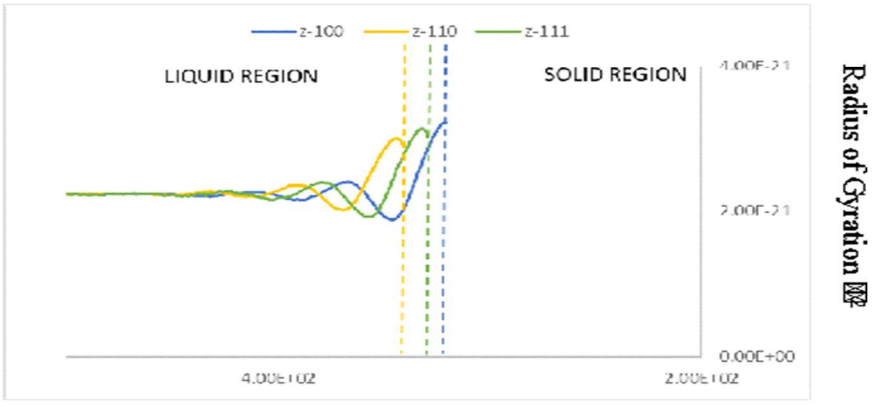

(c)

Figure 4.6 radius of gyration on x-axis (a), y-axis (b), and z-axis (c) for Pentane C_5H_{12} contacting crystal plane of (100), (110), (111)

Figure 4.5 and Figure 4.6 show the radius of gyration in the -x, -y and -z axes for liquid alkanes of C_4H_{10} and C_5H_{12}. Based on both figures, the x-axis is shown in Figure 4.5 (a) and Figure 4.6 (a) for the three types of crystal planes. Where the y-axis is shown in Figure 4.5 (b) and Figure 4.6 (b). Conversely, the z-axis is shown in Figure 4.5 (c) and Figure 4.6 (c). The x and y-components of the radius of gyration have similar trends, i.e., it starts with constant value on the bulk-like region, fluctuates in the layered region, and increases to the maximum value near the solid wall surface. In Figure 4.5 (a) and Figure 4.6 (a) of C_4H_{10} and C_5H_{12} liquid, a remarkable increase of the value of x-axes is observed in the vicinity of the solid surface for the case of crystal plane 110. This phenomenon of exclusively large x-axes disappears in the cases of C_5H_{12} in Figure 4.5 (a) and Figure 4.6 (a), Although the peak heights of the radius of gyration for the (100) and (111) crystal planes are similar, the (110) crystal plane had a higher peak height on C_4H_{10}. However, crystal plane (111) is highest among (100) and (110) for liquid C_5H_{12}. It shows the higher peak on the (110) for C_4H_{10} and (111) for C_5H_{12} introduces an interesting difference since it signifies a unique behaviour of liquid butane and pentane molecules when positioned on this surface.

The elevated peak suggests that liquids C_4H_{10} on crystal plane (110) and C_5H_{12} on plane (111) molecules assume an extended arrangement along the x-axes differentiating their behaviour from crystal planes (100) and (111) for butane C_4H_{10} and plane (100), (110) for pentane C_5H_{12}. This difference in performance may be due to various factors. One possible explanation can be the unique atomic arrangement of the (110) plane for C_4H_{10} and plane (111) for C_5H_{12}, which can provide more available space and encourage liquid molecules to spread out and align along the x-axes. The same radius of gyration profile was observed in previous research papers from (Saleman et al., 2019). However, the researchers did not investigate the decomposed components of the radius of gyration. Based on our results for the y-axes and z-axes, the radius of gyration profile exhibited similar outcomes regardless

of the crystal planes. While for the x-axes, on C_4H_{10} the (110) crystal plane and C_5H_{12} the (111) plane attained the highest value compared to other crystal plane on both liquids. This indicates that the alkane liquid was absorbed in the crystal structure of the (110) plane for C_4H_{10} and (111) for C_5H_{12} on the x-axes. Based on the surface structure of (110) for C_4H_{10} and (111) for C_5H_{12} elongated holes exist along the x-axes, which confirms that these holes were engaged by the liquid alkanes for C_4H_{10} and C_5H_{12} molecules.

4.2.3 Orientation Order Parameter

Orientation order parameter specifies the molecular orientation of liquid on solid surfaces. The orientation order parameter measures the alignment of molecules within a system, ranging from -0.5 to 1.0. A value of -0.5 indicates a perfect parallel orientation of the molecules relative to the S-L interface, while a value of 1.0 signifies a perfect normal orientation. A value of 0 suggests that the molecules are randomly oriented without any preferred alignment (Chilukoti et al., 2014; Wang et al., 2022).

In this study, the data collection region was divided into slabs approximately 0.01 Å thick along the z-direction. The results revealed a consistent orientation order parameter profile, regardless of the length of the liquid alkane molecules. Therefore, Figure 4.7 presents the orientation order parameter of liquid alkanes C_4H_{10} (a) and C_5H_{12} (b) on the FCC (100) surface, as representative data. The trends observed for other FCC crystal planes, (110) and (111), were found to be similar and are thus provided in appendix for reference.

The primary difference in the orientation order parameter among the liquid alkanes lies in the peak height observed in the adsorption layer, which decreases as the alkane chain length increases. On both sides of the solid walls in the system, the orientation order parameter profiles remain consistent. Regardless of the length of the alkane molecules or their interaction with the three FCC crystal planes, most liquid alkane molecules in the adsorption layer are oriented parallel to the solid wall surface. In contrast, molecules in the

bulk-like region exhibits a random orientation. Between the first adsorption layer and the second liquid layer, the molecules tend to align normal to the interface, likely due to their bridging between the two layers. Previous studies observed a pronounced peak in the orientation order parameter at the first adsorption layer adjacent to the solid interface, indicating a strong preferential (parallel) alignment of alkane molecules.

Conversely, in the bulk-like region far from the surface, the values decay to near zero, reflecting random, isotropic molecular orientation (Saleman et al., 2025). In both studies, a pronounced peak appears in the orientation order parameter profiles at the first adsorption layer adjacent to the solid interface, indicating a strong preferential (parallel) orientation of alkane molecules. Conversely, in the bulk-like region far from the surface, the orientation order parameter profile decays to near zero, consistent with random, isotropic molecular orientations in both simulations.

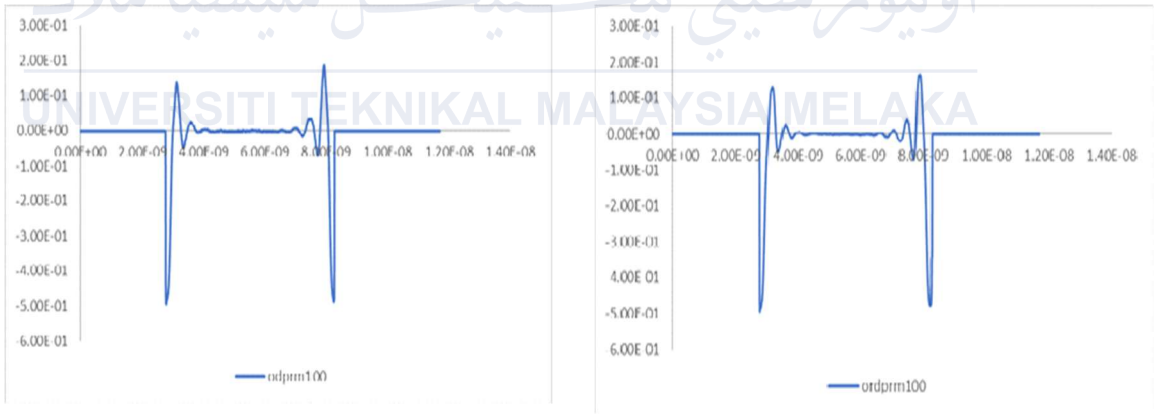

a) b)

Figure 4.7 Orientation order parameter C_4H_{10} contacting (100) (a)crystal plane and C_5H_{12} contacting (100) (b) crystal plane

4.3 Heat Transport Analysis

The analysis of temperature distribution across the S-L interfaces provides valuable insights into the heat transfer mechanisms, particularly in the context of temperature discontinuity and thermal boundary resistance. The temperature discontinuity at the S-L interfaces, combined with the density distribution in the liquid region, plays a crucial role in

determining the heat flux characteristics for C_4H_{10} and C_5H_{12} across different FCC crystal planes of (100), (110), and (111).

4.3.1 Temperature distributions

Figure 4.8 shows the temperature distributions of liquid C_4H_{10} and C_5H_{12} contacting solid surfaces of (100), (110) and (111) imposed on the density distributions. Figure 4.8 (a), (b) and (c) represents the C_4H_{10}contacting solid surfaces of (100), (110) and (111), respectively. Whereas (d), (e) and (f) represent the temperature distributions for C_5H_{12} liquid contacting solid surfaces of (100), (110) and (111), respectively. Here the temperature is calculated based on slab divided based on the layers of solid and liquid adsorption layers. The temperature is calculated based on the microscopic velocity of molecules present in each slab.

As shown in Figure 4.8, only the orientation order parameter profiles for C_4H_{10} on the (100) (a) surface and C_5H_{12} on the (100) (b) are presented. The corresponding results for the (110) and (111) crystal planes are provided in appendix for reference, as they exhibit similar trends. All the temperature profile is observed for all cases of liquid and solid surfaces, where a high temperature is observed on the left side and a low temperature is observed on the right side. This kind of profile is expected since in the simulation system, on the left side, a high temperature is set at approximately the critical temperature of the liquid. On the other hand, on the right side, a low temperature is set at approximately the triple point temperature of the liquids. The existence of temperature difference between the two solid surfaces shows that there exists a constant heat flux in the directions of higher temperature to the lower temperature. Similar findings have been reported in studies of heat transfer in liquid-solid systems, where critical and triple point temperatures serve as boundary conditions from (Zhang et al., 2025).

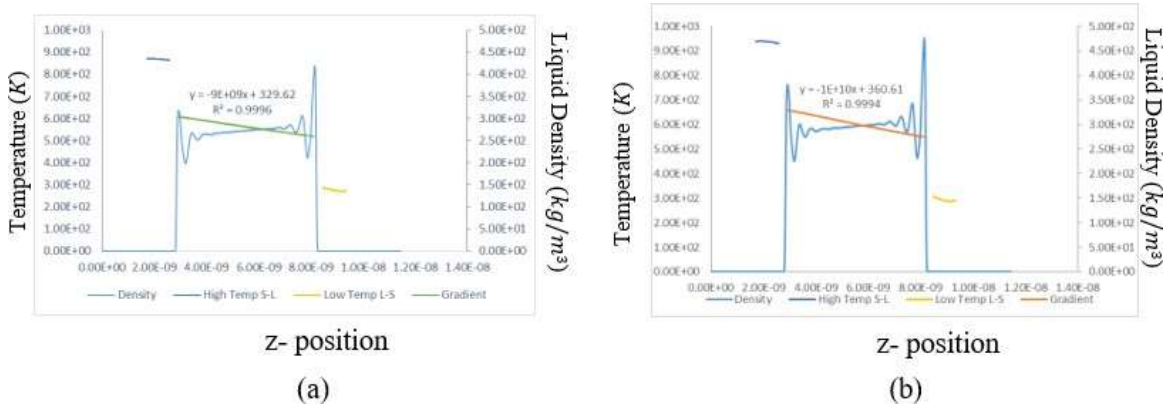

Figure 4.8 Temperature distribution of C_4H_{10} contacting (a) (100) crystal plane and C_5H_{12} contacting (b) (100) crystal plane

Based on Figure 4.8 it is found that there exists a significant temperature discontinuity at the S-L interfaces on the left and right sides of the system. The temperature discontinuity is observed for all cases of liquid and solid surfaces. To further clarify the temperature discontinuity, a temperature difference between solid and liquid is calculated and plotted in Table 4.1. The temperature difference between the solid and liquid is referred to as the temperature jump (TJ).

Table 4.1 shows the temperature jump for liquid C_4H_{10} and C_5H_{12}. Based on the table it is found that difference surface structure and different liquid alkanes exhibits different value of TJ. In this case on average all C_4H_{10} contacting any solid surfaces has lower TJ as compared to C_5H_{12}. Based on Table 4.1, regardless of the liquid alkanes, the solid surfaces of (110) has the lowest value of TJ. However, a slight difference is observed between C_4H_{10} and C_5H_{12} for solid surfaces of (111) and (100), where for C_4H_{10} solid surfaces of (100) has almost similar value to (110). And for the cases of C_5H_{12}, solid surfaces of (111) has lower value followed by solid surfaces of (100). This kind of differences in the TJ will be further elaborated in the heat flux and thermal boundary resistance sections since both of this are contributing to the heat transport across the S-L interfaces.

These temperature gradients create a steady-state heat flux from the higher-

temperature region to the lower-temperature region, demonstrating the fundamental principles of thermodynamic energy transfer (Saleman et al., 2017). (Schmitt et al., 2022) demonstrated that temperature discontinuities (ΔT) and interfacial thermal resistance at liquid–solid interfaces are highly sensitive to both fluid properties and surface structure, emphasizing that solid surface orientation and molecular size strongly modulate heat transfer efficacy. These findings align with recent observations across FCC planes and alkane chain lengths, the (110) surface consistently exhibits the lowest temperature jump, with variations across (100) and (111) corresponding to molecular size and crystal plane orientations.

Table 4.1 Temperature Jump and average on (C_4H_{10}) and (C_5H_{12}) at each FCC (100), (110) and (111)

Alkane	FCC Plane	TJ-left	TJ-right	Average
Butane (C_4H_{10})	100	134.81	148.23	141.52
	110	130.82	143.28	137.05
	111	133.69	148.18	140.94
Pentane (C_5H_{12})	100	167.93	139.69	153.81
	110	164.35	134.28	149.32
	111	167.31	139.47	159.39

4.3.2 Heat flux

Heat flux can be calculated using a modified form of the Irving–Kirkwood equation. Given our system's uniformity and absence of macroscopic fluid motion, we simplified the original expression to obtain instantaneous heat flux, incorporating both energy transported by molecular movement and intermolecular-force transfer consistent with prior frameworks (Fujiwara and Shibahara, 2022).

Understanding heat flux at solid–liquid interfaces is crucial for optimizing thermal transport. This study investigates heat flux at the contact interfaces of (C_4H_{10}) and (C_5H_{12}) across FCC crystal planes (100), (110), and (111), focusing on the influence of temperature discontinuity and thermal boundary resistance. Table 4.2 lists the computed heat flux values: the (100) plane shows the highest values, with C_4H_{10} at $8.38 \times 10^8\ W/m^2$ and C_5H_{12} at

$1.02 \times 10^9\ W/m^2$. This efficient heat transfer is attributed to minimal temperature discontinuity and low boundary resistance. Recent work by (Fujiwara and Shibahara, 2022) also supports this approach by used subatomic-resolution MD to map the directional components of heat flux and stress across solid–liquid interfaces, revealing that energy transport at the interface strongly depends on interaction strength and local interfacial structure, both of which are captured by the Irving–Kirkwood-based heat flux. Their findings reinforce our method and underline how crystal plane surface orientation and local molecular alignment influence thermal conduction.

Understanding heat flux at S-L interfaces is crucial for optimizing thermal transport at S-L interfaces. This study investigates the heat flux at the contact interfaces of C_4H_{10} and C_5H_{12} across FCC crystal planes (100), (110), and (111), focusing on the influence of temperature discontinuity and thermal boundary resistance. Table 4.2 tabulated the heat flux value across the temperature differences for both liquid alkanes. The (100) plane exhibits the highest heat flux values, with C_4H_{10} $8.38\times10^8\ W/m^2$ and (C_5H_{12}) $1.02\times10^9\ W/m^2$. The efficiency of thermal transport are attributed by minimal temperature discontinuity, and low thermal boundary resistance. The molecular configuration and alignment on this plane likely enhance energy transfer efficiency, making it the most favorable for heat conduction thus further analysis is needed to verify the statement.

Table 4.2 Average heat flux for (C_4H_{10}) and (C_5H_{12}) at each FCC (100), (110), and (111) planes

HEATFLUX		
FCC Plane	C4H10	C5H12
100	8.38×10^8 W/m^2	1.02×10^9 W/m^2
110	8.34×10^8 W/m^2	9.06×10^8 W/m^2
111	8.02×10^8 W/m^2	9.99×10^8 W/m^2

The consistent trend across all planes reveals that C_4H_{10} exhibits higher heat flux than butane, regardless of the crystallographic orientation. This is likely due to the differences in molecular structure and interaction dynamics, which enhance C_5H_{12} thermal conductivity. Moreover, the variations in heat flux between planes emphasize the role of crystallographic orientation in dictating thermal transport properties. Temperature discontinuity at the interface serves as a key factor influencing thermal boundary resistance. The lower the discontinuity, the higher the efficiency of energy transfer across the interface. The (100) plane's optimal molecular alignment minimizes this discontinuity, while the (111) plane's structure creates barriers to heat flow, exacerbating resistance.

Previous research (Saleman et al., 2017), examines the thermal transport properties and structural characteristics of S-L interfaces between FCC crystal planes and linear alkane liquids, highlighting the influence of molecular structure on heat transfer. While (Saleman et al., 2017) performed nonequilibrium molecular dynamics across a broad range of alkane chain lengths (up to C_{24}) and various FCC surface orientations to investigate thermal boundary resistance, this study focuses specifically on a comparison of both C_4H_{10} and C_5H_{12} interacting with (100), (110), and (111) surfaces. Furthermore, the analysis correlates these heat flux values with observed temperature jumps, revealing that pentane consistently transfers heat more efficiently than butane, and that the (100) surface with its favorable molecular alignment exhibits the lowest interfacial resistance. These plane specifically insights linking molecular structure and crystal plane orientation to actual thermal transport performance constitute the importance contribution of this work.

4.3.3 Thermal Boundary Resistance (TBR)

Table 4.3 tabulated the temperature jump at each interface on the 0.75Tc, and 0.65Tc, sides and the heat flux of the system. From the average temperature jump and the heat flux, thermal boundary resistance (TBR) at the S-L interface was calculated by (Anandakrishnan

and Sathian, 2023) demonstrates the same formalism TBR is obtained directly from the interfacial temperature discontinuity and heat flux measured in molecular dynamics simulations of solid–liquid systems. Their data-driven analysis revealed that interfacial liquid layering and surface wettability strongly correlate with TBR. Based on Table 4.3 ΔT is the average temperature jump across S-L interfaces, and J is the heat flux across the simulation system. The TBR is the ratio between the temperature jump over the heat flux across the simulation system.

From the provided data, we observe distinct differences in TBR between C_4H_{10} and C_5H_{12} across various crystal planes. For example, for the crystal plane of (100), C_4H_{10}exhibits a TBR value of 5.92×10^6 m²K/W, while C_5H_{12} shows a significantly higher value of 6.62×10^6 m²K/W. Similarly, at (110), C_4H_{10} TBR is 6.08×10^6 m²K/W compared to C_5H_{12} 6.07×10^6 m²K/W, and at (111), the values are 5.75×10^6 m²K/W for C_4H_{10} and 6.51×10^6 m²K/W forC_5H_{12}.

Analyzing these numerical values reveals that C_5H_{12} consistently exhibits higher TBR than C_4H_{10} across all crystal planes studied. This finding directly correlates with the research objectives, emphasizing the importance of structural properties in influencing interfacial thermal resistance. The higher TBR values in C_5H_{12} suggest stronger adsorption interactions and greater structural properties at the interface.

In conclusion, the comparative analysis of interfacial thermal resistance between $C_4H_{10}$and C_5H_{12}across different crystal planes highlights the significant role of molecular adsorption and structural properties in heat transport. This study supports the overarching objective of correlating molecular-level phenomena with TBR, paving the way for innovations in material design and thermal management.

Table 4.3 Average value for heat flux, temperature jump, and thermal boundary resistance on C_4H_{10} and C_5H_{12} contacting each of FCC (100), (110) and (111)

Alkane	FCC Plane	Heat Flux (J) W	Temperature Jump (TJ) K	Thermal Boundary Resistances (TBR)
Butane, (C_4H_{10})	100	8.38×10^8	142	5.92×10^6
	110	8.34×10^8	137	6.08×10^6
	111	8.02×10^8	141	5.69×10^6
Pentane, C_5H_{12})	100	1.02×10^9	154	6.62×10^6
	110	9.06×10^8	149	6.07×10^6
	111	9.99×10^8	159	6.51×10^6

4.3.4 Validation of the heat transport results

In order to validate the results of the thermal heat flux across the simulation system, the thermal conductivity of the liquid measure through the simulation systems is compared to the experimental data of previous researchers. Table 4.4 shows the value of thermal conductivity of liquid C_4H_{10} and C_5H_{12}. Based on Table 4.4, the MD simulations proved quite accurate, with results differing from experimental data by less than 15% for both liquids, which is in fair agreement. This close agreement validates that the MD simulation method can effectively predict thermal conductivity in these liquid alkanes. The past experiment paper for C4H10 validated from (Shibahara and Takeuchi, 2011; Vassiliou et al., 2015)

Table 4.4 Thermal Conductivity on butane (C_4H_{10}) and pentane (C_5H_{12})

Alkane		Experiment	Present Simulation	Deviation in percentage (%)
C_4H_{10}	274	$9.34 \text{ X } 10^{-2}$	$8.31 \text{ X } 10^{-2}$	11
C_5H_{12}	297	$9.50 \text{ X } 10^{-2}$	$8.20 \text{ X } 10^{-2}$	13

CHAPTER 5

CONCLUSION AND RECOMMENDATIONS FOR FUTURE RESEARCH

5.1 Conclusion

The present study conducted a detailed investigation of the behaviour of liquid alkanes of butane (C_4H_{10}) and pentane (C_5H_{12}) at solid surfaces of FCC crystal planes (100), (110), and (111) using molecular dynamics simulations. The results highlight the significant influence of crystal planes on the structural quantities and thermal transport mechanisms of the alkane liquid on solid surfaces.

The first objective of this study was to clarify the adsorption mechanisms of liquid hydrocarbons of C_5H_{12} and C_4H_{10} on solid surfaces using molecular dynamics (MD) simulations. To achieve this, key structural quantities, namely density distribution, orientation order parameter, and radius of gyration, were analysed in detail. The density distribution analysis revealed structured adsorption layers near the solid surfaces, with peak densities varying across crystal planes. The (111) plane exhibited the highest adsorption density, as compared to other FCCs. The radius of gyration analysis emphasised the role of crystal orientation in shaping molecular structures, with distinct behaviour observed along the x-axis for butane and pentane on the (110) plane. Structural quantities confirmed that hydrocarbon molecules predominantly align parallel to the solid surfaces in the adsorption layer, transitioning to random orientations in the bulk-like regions. These structural adaptations were consistent across different crystal planes and reflected the impact of alkane chain length orientations.

The second objective aimed to identify the heat flux at the solid-liquid (S-L) interfaces by assessing the temperature discontinuity and thermal boundary resistance (TBR). Without considering the (110) plane, the (111) plane emerged as the most effective for heat conduction due to its low TBR, while the (100) plane showed greater TBR. The

(110) exhibits anomaly TBR, as for C_4H_{10} it has the highest TBR, whereas in C_5H_{12} it has the lowest TBR. Overall, C5H12 exhibited higher heat flux than C4H10 across all planes.

5.2 Limitations of the Present Study

The study uses molecular dynamics simulations that assume idealised conditions, such as constant temperatures and periodic boundary conditions, which may not fully capture real-world complexities. The interactions of free electrons in gold are not considered in the simulation, which might influence heat conduction behaviour at the solid-liquid interface. The study focuses only on C_4H_{10} and C_5H_{12}, limiting the generalisation of results to other liquid hydrocarbons or complex molecular systems. The simulations are conducted within a specific temperature range (0.75Tc) and (0.65Tc), which might not encompass broader thermal behaviours relevant to industrial applications.

5.3 Future Recommendations

For future studies focusing on (C_4H_{10}) and (C_5H_{12}), several recommendations can enhance the understanding of their molecular behaviour and interactions on FCC surfaces. Firstly, extending the study to include a wider range of temperatures and pressures can provide a more comprehensive view of how these conditions affect the density distributions, radius of gyration, order parameters, temperature profiles, heat flux, and TBR. Exploring extreme conditions could reveal critical insights into phase transitions and stability limits.

Experimental validation of the simulation results through techniques like neutron scattering, X-ray diffraction, or atomic force microscopy would be beneficial. Collaborating with experimentalists to compare theoretical predictions with real-world data can strengthen the study's findings and provide a more robust understanding of molecular interactions on FCC surfaces.

Lastly, exploring the dynamic behaviour of butane and pentane on FCC surfaces

under nonequilibrium conditions, such as during rapid heating or cooling, could provide insights into transient phenomena and relaxation processes. Understanding these dynamics is crucial for applications involving rapid thermal cycling or thermal management. By addressing these aspects, future studies can significantly advance the understanding of (C_4H_{10}) and (C_5H_{12}) behaviour on FCC surfaces, paving the way for optimized material design and novel applications in various fields.

REFERENCES

Abreu, C.R.A., Tuckerman, M.E., 2021. Multiple timescale molecular dynamics with very large time steps: avoidance of resonances. European Physical Journal B. https://doi.org/10.1140/epjb/s10051-021-00226-4.

Aldossary, O.M., 2021. Generalized non-integer Lennard-Jones potential function vs. generalized Morse potential function for calculating cohesive energy and melting point of nanoparticles. J King Saud Univ Sci 33. https://doi.org/10.1016/j.jksus.2020.101316

Aldossary, O.M., Al Rsheed, A., 2020. A New Generalized Morse Potential Function for Calculating Cohesive Energy of Nanoparticles. Energies (Basel) 13. https://doi.org/10.3390/en13133323.

Anandakrishnan, A., Sathian, S.P., 2023. A data driven approach to model thermal boundary resistance from molecular dynamics simulations. Physical Chemistry Chemical Physics 25. https://doi.org/10.1039/d2cp04551f.

Assaf, E.I., Liu, X., Lin, P. and Erkens, S. 2024 Introducing a force-matched united atom force field to explore larger spatiotemporal domains in molecular dynamics simulations of bitumen. Materials and Design, 240, 112831. https://doi:10.1016/j.matdes.2024.112831.

Boone, P., Babaei, H., Wilmer, C.E., 2019. Heat Flux for Many-Body Interactions: Corrections to LAMMPS. J Chem Theory Comput 15. https://doi.org/10.1021/acs.jctc.9b00252.

Castro Anaya, L.E., Gómez, S.Y. and Orozco, G.A. 2023. Comprehensive Automated Routine Implementation, Validation, and Benchmark of the Anisotropic Force Field (AUA4) Using Python and GROMACS, Journal of Physical Chemistry A, 127(6), pp.1555–1563. doi:10.1021/acs.jpca.2c08335.

Chang, S.W., Chiang, K.F., Cai, W.L., 2019. Thermal performance evaluation of thin vapor chamber. Appl Therm Eng 149.

Chang, Q., Huang, L., McKenzie, K., Carere, C., Stott, M., Nicol, A. and Dempsey, D. 2024. Influence of hydrogen sulfide on gas-water interface in underground hydrogen storage: A molecular dynamics study, Journal of Energy Storage, 97, 112766. doi: 10.1016/j.est.2024.112766.

Chen, L., Qian, L., 2021. Role of interfacial water in adhesion, friction, and wear—A critical review. Friction. https://doi.org/10.1007/s40544-020-0425-4.

Chen, Z., Lu, Y., Li, R., Li, D., Xiang, B., Li, J., Liu, Q., 2023. Liquid-solid contact electrification through the lens of surface and interface science. Nano Energy 116. https://doi.org/10.1016/j.nanoen.2023.108834.

Chilukoti, H.K., Kikugawa, G., Ohara, T., 2014. Structure and transport properties of liquid alkanes in the vicinity of α-quartz surfaces. Int J Heat Mass Transf 79. https://doi.org/10.1016/j.ijheatmasstransfer.2014.08.089.

Chilukoti, H.K., Kikugawa, G., Ohara, T., 2013. A molecular dynamics study on transport properties and structure at the liquid-vapor interfaces of alkanes. Int J Heat Mass Transf 59. https://doi.org/10.1016/j.ijheatmasstransfer.2012.12.015.

Ciccotti, G., Decherchi, S., Meloni, S., 2025. Foundations of molecular dynamics simulations: how and what. La Rivista del Nuovo Cimento. https://doi.org/10.1007/s40766-025-00065-4.

Corral-Casas, C., Ayestarán Latorre, C., Gattinoni, C., Brewer, M., Karl, J., Dini, D., Ewen, J.P., 2025. Molecular Insights into the Adsorption of Deposit Control Additives from Hydrocarbon Fuels. Langmuir 41, pp. 1900–1913. https://doi.org/10.1021/acs.langmuir.4c04368.

Cui, Y., Qin, Z., Wu, H., Li, M., Hu, Y., 2021. Flexible thermal interface based on self-assembled boron arsenide for high-performance thermal management". Nat Commun 12. https://doi.org/10.1038/s41467-021-21531-7.

da Silva, G.C.Q., Silva, G.M., Tavares, F.W., Fleming, F.P., Horta, B.A.C., 2022. Are all- atom any better than united-atom force fields for the description of liquid properties of alkanes: A systematic study considering different chain lengths. J Mol Liq 354. https://doi.org/10.1016/j.molliq.2022.118829

Deng, S., Xiao, C., Yuan, J., Ma, D., Li, J., Yang, N., He, H., 2019. Thermal boundary resistance measurement and analysis across SiC/SiO2 interface. Appl Phys Lett 115. https://doi.org/10.1063/1.5111157.

Dong, M., Xu, J., Wang, Y., Liu, G., 2024. Effect of Pressure and Surface Wettability on Thermal Resistance across Solid-Liquid Interface in Supercritical Regime. Journal of Physical

Chemistry C 128. https://doi.org/10.1021/acs.jpcc.3c07909

Dong, Y., Wang, L., Wei, C., 2022. Characterization of Liquid-Vapor Interfaces in Pores During Evaporation. Water Resour Res 58. https://doi.org/10.1029/2021WR031908.

Du, R., Zhang, A., Du, Z., Zhang, X., 2020. Molecular dynamics simulation on thin-film lubrication of a mixture of three alkanes. Materials 13. https://doi.org/10.3390/MA13173689.

El-Rifai, A., Perumanath, S., Borg, M.K., Pillai, R., 2024. Unraveling the Regimes of Interfacial Thermal Conductance at a Solid/Liquid Interface. Journal of Physical Chemistry C 128, pp. 8408–8417. https://doi.org/10.1021/acs.jpcc.4c00536.

El-Rifai, A., Klochko, L., Perumanath, S., Lacroix, D., Pillai, R. and Isaiev, M. 2025. Spectral mechanisms of solid/liquid interfacial heat transfer in the presence of a meniscus. Physical Chemistry Chemical Physics, 27, pp. 10185–10197. doi:10.1039/D4CP04768K.

Estrada, E., 2004. Three-dimensional generalized graph matrix, Harary descriptors, and a generalized interatomic Lennard-Jones potential. Journal of Physical Chemistry A 108. https://doi.org/10.1021/jp049139c.

Feng, C.P., Bai, L., Bao, R.Y., Wang, S.W., Liu, Z., Yang, M.B., Chen, J., Yang, W., 2019. Superior thermal interface materials for thermal management. Composites Communications 12. https://doi.org/10.1016/j.coco.2019.01.003.

Frenkel, D., Smit, B., 2023. Understanding Molecular Simulation: From Algorithms to Applications, Third Edition", https://doi.org/10.1016/C2009-0-63921-0

Fujiwara, K., Shibahara, M., 2022. Thermal transport mechanism at a solid-liquid interface based on the heat flux detected at a subatomic spatial resolution. Phys Rev E 105. https://doi.org/10.1103/PhysRevE.105.034803.

Fujiwara, K., Shibahara, M., 2019. Atomic-scale thermal manipulation with adsorbed atoms on a solid surface at a liquid-solid interface. Sci Rep 9. https://doi.org/10.1038/s41598-019-49677-x.

Ghatage, D., Tomar, G., Shukla, R.K., 2020. Thermostat-induced spurious interfacial resistance in non-equilibrium molecular dynamics simulations of solid-liquid and solid- solid systems. Journal of Chemical Physics 153. https://doi.org/10.1063/5.0019665.

Giri, A., Walton, S.G., Tomko, J., Bhatt, N., Johnson, M.J., Boris, D.R., Lu, G., Caldwell, J.D., Prezhdo, O. V, Hopkins, P.E., 2023. Ultrafast and Nanoscale Energy Transduction Mechanisms and Coupled Thermal Transport across Interfaces. ACS Nano. https://doi.org/10.1021/acsnano.3c02417.

Gisbert, A.T., Piovella, N., 2020. Multimode collective atomic recoil lasing in free space. Atoms 8. https://doi.org/10.3390/atoms8040093.

Goga, N., Mayrhofer, L., Tranca, I., Nedea, S., Heijmans, K., Ponnuchamy, V., Vasilateanu, A., 2021. A review of recent developments in molecular dynamics simulations of the photoelectrochemical water splitting process. Catalysts. https://doi.org/10.3390/catal11070807.

Guo, Y., Surblys, D., Kawagoe, Y., Matsubara, H., Liu, X., Ohara, T., 2019a. A molecular dynamics study on the effect of surfactant adsorption on heat transfer at a solid-liquid interface. Int J Heat Mass Transf 135. https://doi.org/10.1016/j.ijheatmasstransfer.2019.01.131

Guo, Y., Surblys, D., Kawagoe, Y., Matsubara, H., Ohara, T., 2019b. A molecular dynamics study of heat transfer over an ultra-thin liquid film with surfactant between solid surfaces. J Appl Phys 126. https://doi.org/10.1063/1.5123583.

Ghahremanpour, M.M., Tirado-Rives, J. and Jorgensen, W.L. 2022. Refinement of the Optimized Potentials for Liquid Simulations Force Field for Thermodynamics and Dynamics of Liquid Alkanes. Journal of Physical Chemistry B, 126(31), pp. 5896– 5907. doi: 10.1021/acs.jpcb.2c03686.

Govorun, E.N., Dupré de Baubigny, J., Perrin, P., Reyssat, M., Pantoustier, N., Salez, T. and Monteux, C. 2024. Growth of membranes formed by associating polymers at interfaces. Soft Matter, 20, pp. 6822–6833. doi: 10.1039/D4SM00563E.

Hadjiconstantinou, N.G., Swisher, M.M., 2022. An atomistic model for the thermal resistance of a liquid-solid interface. J Fluid Mech 934. https://doi.org/10.1017/jfm.2021.1136

Hamal, P., Subasinghege Don, V., Nguyenhuu, H., Ranasinghe, J.C., Nauman, J.A., McCarley, R.L., Kumar, R., Haber, L.H., 2021. Influence of Temperature on Molecular Adsorption and Transport at Liposome Surfaces Studied by Molecular Dynamics Simulations and Second Harmonic Generation Spectroscopy. Journal of Physical Chemistry B 125, pp. 10506–10513. https://doi.org/10.1021/acs.jpcb.1c04263.

Harrison, J.A., Schall, J.D., Maskey, S., Mikulski, P.T., Knippenberg, M.T., Morrow, B.H.,

2018. Review of force fields and intermolecular potentials used in atomistic computational materials research. Appl Phys Rev. https://doi.org/10.1063/1.5020808.

Humphreys, D.D., Friesner, R.A., Berne, B.J., 1994. A multiple-time-step Molecular Dynamics algorithm for macromolecules. Journal of Physical Chemistry 98. https://doi.org/10.1021/j100078a035.

Hrahsheh, F. and Wilemski, G. 2023. Effects of molecular size and orientation on the interfacial properties and wetting behaviour of water/n-alkane systems: a molecular- dynamics study. Physical Chemistry Chemical Physics, 25(7), pp. 5808–5816. doi: 10.1039/D2CP05735B.

Islam, M.A., Rahman, S.M.M., Mim, J.J., Khan, S., Khan, F., Patwary, M.A.I., Hossain, N., 2025. Applications of molecular dynamics in nanomaterial design and characterization - A review. Chemical Engineering Journal Advances. https://doi.org/10.1016/j.ceja.2025.100731.

Issa, K.M., Mohamad, A.A., 2012. Lowering liquid-solid interfacial thermal resistance with nanopatterned surfaces. Phys Rev E Stat Nonlin. Soft Matter Phys 85. https://doi.org/10.1103/PhysRevE.85.031602.

Ishihara, K. and Kaji, H. 2024. Predictions of molecular orientation and charge mobility in organic vacuum-deposited thin films by multiscale simulation. Communications Materials. https://doaj.org/article/37ca9e3b2ce643bc83213d64758c8646

Ito, T., Matsubara, H., Surblys, D., Ohara, T., 2022. Molecular dynamics study on the thermal conductivity of a single polyethylene chain: Strain dependence and potential models' effect. AIP Adv 12. https://doi.org/10.1063/5.0095975.

Jang, S., Kim, D., Lee, Y., 2025. Advancing Vapor-Liquid Equilibrium Predictions with the OPPES United Atom Forcefield for Associating Fluids. https://doi.org/10.21203/rs.3.rs-7053206/v1.

Jiang, W., Hou, Z., Wu, X., Gai, J., Zheng, L., Wang, Yunchao, Nie, C., Lu, S., Su, Xu, Zhou, J., Yan, S., Yang, E., Huang, B., Dong, C., Sun, J., Su, L., Yao, S., Wang, Yane, Yu, X., Liu, D., Jiang, J., Wu, J., Fu, X., Wang, S., Su, Xueying, Shan, H., Zhang, L., Qi, G., He, X., Li, J., Ma, Y., Wang, Yongping, 2025. Frontier advances in molecular dynamics simulations for the design and optimization of oil-displacement polymers. RSC Adv. https://doi.org/10.1039/d5ra00059a

Knudsen, P.A., Heyes, D.M., Niss, K., Dini, D. and Bailey, N.P. 2024. Invariant dynamics in

a united-atom model of an ionic liquid. Journal of Chemical Physics, 160(3), Article 034503. doi: 10.1063/5.0177373.

Khan, I., Haghmoradi, A., Sedghi, M. and Panagiotopoulos, A.Z. 2022. Comparison of the United- and All-Atom Representations of (Halo) alkanes. Journal of Chemical Theory and Computation, 18(11), pp. 6784–6799. doi: 10.1021/acs.jctc.2c00524.

Klochko, L., Mandrolko, V., Castanet, G., Pernot, G., Lemoine, F., Termentzidis, K., Lacroix, D., Isaiev, M., 2023. Molecular dynamics simulation of thermal transport across a solid/liquid interface created by a meniscus. Physical Chemistry Chemical Physics 25. https://doi.org/10.1039/d2cp04601f.

Kumar, R., Hussainova, I., Rahmani, R., Antonov, M.,. 2022. Solid Lubrication at High-Temperatures - A Review. Materials. https://doi.org/10.3390/ma15051695.

Kurzawski, A.J., Ezekoye, O.A., 2020. Inversion for fire heat-release rate using heat flux measurements. J Heat Transfer 142. https://doi.org/10.1115/1.4046264.

Laurent, A.A., 2019. Review of Algorithms Used in Molecular Dynamics Simulations. Undergraduate Research in Natural and Clinical Sciences and Technology Journal. https://doi.org/10.26685/urncst.157.

Langer, M.F., Knoop, F., Carbogno, C., Scheffler, M. and Rupp, M. 2023. Heat flux for semilocal machine-learning potentials. Physical Review B, 108, L100302. doi: 10.1103/PhysRevB.108.L100302.

Li, C.-Y., Huang, J.-H., Li, H. and Luo, M.-B. 2020. Study on the interfacial properties of polymers around a nanoparticle. RSC Advances, 10, pp. 28075–28083. doi: 10.1039/D0RA05392A.

Lin, S., Chen, X., Wang, Z.L., 2022. Contact Electrification at the Liquid-Solid Interface. Chem Rev. https://doi.org/10.1021/acs.chemrev.1c00176

Liu, C., Tian, Y., Meng, Y.,. 2021. A Chemical Potential Equation for Modeling Tribo-electrochemical Reactions on Solid–Liquid Interfaces. Front Chem 9. https://doi.org/10.3389/fchem.2021.650880.

Luo, Q.Y., Surblys, D., Matsubara, H., Ohara, T.,. 2024. Chemical heterogeneity size effects at nanoscale on interface thermal resistance of solid-liquid polymer interface via molecular

dynamics simulations. AIP Adv 14. https://doi.org/10.1063/5.0218506.

Ma, H., Gao, B., Wang, M., Yuan, Z., Shen, J., Zhao, J., Feng, Y.,. 2021. Strategies for enhancing thermal conductivity of polymer-based thermal interface materials: a review. J Mater Sci. https://doi.org/10.1007/s10853-020-05279-x.

Math, S., Gao, J., Landman, U.,. 2022. Interfacial Segregation, Structure, and Diffusion of n-Alkane Mixture Films Adsorbed on Smooth and Rough Gold Surfaces. Journal of Physical Chemistry C 126. https://doi.org/10.1021/acs.jpcc.1c10471.

Matsubara, H., Surblys, D., Ohara, T.,. 2023. One-dimensional harmonic chain model of vibration-mode matching in solid-liquid interfacial thermal transport. Phys Rev E 107. https://doi.org/10.1103/PhysRevE.107.024103.

Mandrolko, V., Termentzidis, K., Lacroix, D. and Isaiev, M. 2025. Tailoring heat transfer at silica-water interfaces via hydroxyl and methyl surface groups. arXiv, preprint, 2 May. https://arxiv.org/abs/2505.01141

McCready, C., Sladekova, K., Conroy, S., Gomes, J.R.B., Fletcher, A.J. and Jorge, M. 2024. Quantifying the Uncertainty of Force Field Selection on Adsorption Predictions in MOFs. Journal of Chemical Theory and Computation, 20(11), pp. 4869–4884. doi: 10.1021/acs.jctc.4c00287.

Miao, C., Tang, J., Yang, K., Xiao, N., Shao, Z., Zhang, F., Zhang, H., Xiong, Y., Xiong, B., Chen, H.,. 2024. Recent Progress on the Tribological Applications of Solid Lubricants. J Tribol 146. https://doi.org/10.1115/1.4063701

Mohammadian, B., McCulloch, M.A., Sweetnam, T., Gilles, V., Piccirillo, L., 2024. The Impact of Surface Passivation on Kapitza Resistance at the Interface Between a Semiconductor and Liquid Nitrogen. J Low Temp Phys 214. https://doi.org/10.1007/s10909-023-03020-x.

Martens, C.M. 2024. Semiflexible and charged polymers at interfaces". PhD thesis. Eindhoven University of Technology. https://research.tue.nl/files/337964243/20240918_Martens_hf.pdf

Naga Parameswara Gupta, S., 2022. Basic Nature of intermolecular attraction forces and Comparison with forces like Van Der Waals and hydrogen bonds by Multi Molecule Theory. SCIREA Journal of Mathematics. https://doi.org/10.54647/mathematics11304.

Oliveira, M.P., Gonçalves, Y.M.H., Ol Gheta, S.K., Rieder, S.R., Horta, B.A.C. and Hünenberger, P.H. 2022. Comparison of the United- and All-Atom Representations of alkanes Based on Two Condensed-Phase Force Fields Optimized against the Same Experimental Data Set. Journal of Chemical Theory and Computation, 18(11). pp. 6757–6778. doi: 10.1021/acs.jctc.2c00524.

Peña, J.J., Morales, J., García-Ravelo, J., Avendaño, J., García-Martínez, J., 2021. On the one-dimensional Morse potential as limit of a class of multiparameter exponential-type radial potential. Int J Quantum Chem. https://doi.org/10.1002/qua.26572.

Peterson, J., Russell, J.T., 2025. Modified Morse potentials for classical molecular dynamics simulation of nuclear materials. Nuclear Science and Technology Open Research 3, 16. https://doi.org/10.12688/nuclscitechnolopenres.17651.1.

Qian, C., Wang, Y., He, H., Huo, F., Wei, N., Zhang, S., 2018. Lower Limit of Interfacial Thermal Resistance across the Interface between an Imidazolium Ionic Liquid and Solid Surface. Journal of Physical Chemistry C 122. https://doi.org/10.1021/acs.jpcc.8b06974.

Rafeq Saleman, A., Shukri Zakaria, M., Kejuruteraan Mekanikal, F., Jumaidin, R., Hazwani Mokhtar Fakulti Teknologi Kejuruteraan, N., Aslily Sarkam, N.,. 2022. Molecular Dynamics Study: Correlation of Heat Conduction Across S-L Interfaces Between Constant Heat Flux and Shear Applied to Liquid Systems. Journal of Mechanical Engineering.

Rauscher, P.M., Öttinger, H.C., de Pablo, J.J., 2022. Nonequilibrium statistical thermodynamics of multicomponent interfaces. Proc Natl Acad Sci U S A 119. https://doi.org/10.1073/pnas.2121405119.

Saleman, A.R., Zakaria, M.S., Jumaidin, R., Maslan, M.N., 2021. Ultra-Thin Liquid Film with Shear and the Influences on Thermal Energy Transfer at Solid-Liquid Interfaces of Simple Liquid Methane in Contact With (110) Surface Structure of Face-Centred Cubic Lattice (FCC). Journal of Advanced Research in Fluid Mechanics and Thermal Sciences 87. https://doi.org/10.37934/arfmts.87.3.2130.

Saleman, A.R., Zakaria, M.S., Rosli, M.A.M., Manshoor, B., 2025. Adsorption Mechanism of Linear Alkane Liquid in Contact with Face Centred Cubic Lattice. CFD Letters 17, pp. 1–12. https://doi.org/10.37934/cfdl.17.8.112.

Saleman, A.R. bin, Chilukoti, H.K., Kikugawa, G., Ohara, T., 2019. A molecular dynamics study on the thermal rectification effect at the solid–liquid interfaces between the face-centred cubic (FCC) of gold (Au) with the surfaces of (100), (110) and (111) crystal planes facing the liquid methane (CH4). Mol Simul 45. https://doi.org/10.1080/08927022.2018.1535177.

Saleman, A.R. bin, Chilukoti, H.K., Kikugawa, G., Shibahara, M., Ohara, T., 2017. A molecular dynamics study on the thermal transport properties and the structure of the solid–liquid interfaces between face centered cubic (FCC) crystal planes of gold in contact with linear alkane liquids. Int J Heat Mass Transf 105, pp. 168–179. https://doi.org/10.1016/J.IJHEATMASSTRANSFER.2016.09.069

Saurabh, S., Lei, L., Li, Z., Seddon, J.M., Lu, J., Kalonia, C. and Bresme, F. 2024. Adsorption of monoclonal antibody fragments at the water–oil interface: A coarse- grained molecular dynamics study. APL Bioengineering, 8(2), Article 026128. doi: 10.1063/5.0207959.

Samant, R., Lotliker, S.U., Desai, A.M., 2023. Comments on the paper 'Comparison study of bound states for diatomic molecules using Kratzer, Morse, and modified Morse potentials. Phys Scr. https://doi.org/10.1088/1402-4896/acaa66.

Schmitt, S., Vo, T., Lautenschlaeger, M.P., Stephan, S., Hasse, H., 2022. Molecular dynamics simulation study of heat transfer across solid–fluid interfaces in a simple model system. Mol Phys 120. https://doi.org/10.1080/00268976.2022.2057364.

Shibahara, M., Takeuchi, K., 2011. A molecular dynamics study on the effects of nanostructural clearances on thermal resistance at a lennard-jones liquid-solid interface. Journal of Thermal Science and Technology 6. https://doi.org/10.1299/jtst.6.9

Smardz, P., Anila, M. M., Rogowski, P., Li, M. S., Różycki, B. and Krupa, P. 2024. A Practical Guide to All-Atom and Coarse-Grained Molecular Dynamics Simulations Using Amber and Gromacs: A Case Study of Disulfide-Bond Impact on the Intrinsically Disordered Amyloid Beta. International Journal of Molecular Sciences, 25(12), Article 6698. doi: 10.3390/ijms25126698

Song, L., Zhang, Y., Zhan, J., An, Y., Yang, W., Tan, J., Cheng, L., 2022. Interfacial thermal

resistance in polymer composites: a molecular dynamic perspective. Mol Simul 48. https://doi.org/10.1080/08927022.2022.2071874.

Subramanian, S. and Wang, J.-C. 2005. Anisotropic diffusion of n-butane and n-decane on a stepped metal surface, Journal of Chemical Physics, 123(1), Article 014706. doi: 10.1063/1.1949170.

Tian, S., Dong, Z., Liu, B., Xue, H., Erastova, V., Wang, M., Yan, H., 2022. Characteristics of Gaseous/Liquid Hydrocarbon Adsorption Based on Numerical Simulation and Experimental Testing. Molecules 27. https://doi.org/10.3390/molecules27144590

Torii, D., Ohara, T., Ishida, K., 2010. Molecular-scale mechanism of thermal resistance at the solid-liquid interfaces: Influence of interaction parameters between solid and liquid molecules. J Heat Transfer 132. https://doi.org/10.1115/1.3211856.

Tuckerman, M., Berne, B.J., Martyna, G.J., (1992). Reversible multiple time scale molecular dynamics". J Chem Phys 97. https://doi.org/10.1063/1.463137

Vassiliou, C.M., Assael, M.J., Huber, M.L., Perkins, R.A., 2015. Reference correlations of the thermal conductivity of cyclopentane, iso-pentane, and n-pentane. J Phys Chem Ref Data 44. https://doi.org/10.1063/1.4927095

Vorsmann, C.F., Del Galdo, S., Capone, B. and Locatelli, E. 2024. Colloidal adsorption in planar polymeric brushes. Nanoscale Advances, 6, pp. 816–825. doi: 10.1039/D3NA00598D.

Wan, S., Bhati, A.P., Coveney, P. V., 2023. Comparison of Equilibrium and Nonequilibrium Approaches for Relative Binding Free Energy Predictions. J Chem Theory Comput 19, pp. 7846–7860. https://doi.org/10.1021/acs.jctc.3c00842.

Wang, D., Lippmann, M., Gäding, J., Ehnes, A., Novikov, D., Meißner, R., Seeck, O.H., 2023. Orientation order of a nonpolar molecular fluid compressed into a nanosmall space. Nanoscale 15. https://doi.org/10.1039/d2nr06330a.

Wang, J., Wang, Z., Yang, K., Chen, N., Ni, J., Song, J., Li, Q., Sun, F., Liu, Y., Fan, T., 2022. Enhanced Heat Transport Capability across Boron Nitride/Copper Interface through Inelastic Phonon Scattering. Adv Funct Mater. https://doi.org/10.1002/adfm.202206545

Wang, X., Qiu, S., Wu, J., Abdulagatov, I.M., 2020. Measurements of the Thermal

Conductivity of n-Pentane, Isopentane, 1-Pentene, and 1-Pentanol in the Temperature Range from 253 to 373 K at Pressures up to 30 MPa. J Chem Eng Data 65. https://doi.org/10.1021/acs.jced.9b01147

Wang, J., Devarajan, D.S., Nikoubashman, A. and Mittal, J. 2023. Conformational properties of polymers at droplet interfaces as model systems for disordered proteins. ACS Macro Letters, 12(11), pp. 1472–1478. doi: 10.1021/acsmacrolett.3c00456.

Wang, J. 2023. Conformational properties of polymers at droplet interfaces as model systems for disordered proteins. bioRxiv, preprint posted 29 July. doi: 10.1101/2023.07.29.551102.

Wu, H., Dai, Y., Ding, M.D., 2023. Highly Energetic Electrons Accelerated in Strong Solar Flares as a Preferred Driver of Sunquakes. Astrophys J Lett 943. https://doi.org/10.3847/2041-8213/acb0d1.

Wu, J., Rui, Z., Wang, Z., Dong, Y., 2023. Molecular dynamics study on the thermal conductivity of a single polyethylene chain: Strain dependence and potential models' effect. Journal of Physics Condensed Matter 35. https://doi.org/10.1088/1361- 648X/acbc03.

Xia, S.Y., Guo, L.Y., Tao, L.Q., Long, Y., Huang, Z., Wu, J., Li, J., 2023. Self-Powered Paper-Based Pressure Sensor Driven by Triboelectric Nanogenerator for Detecting Dynamic and Static Forces. IEEE Trans Electron Devices 70. https://doi.org/10.1109/TED.2022.3225129.

Yu, J.J., Tang, R., Li, Y.R., Zhang, L., Wu, C.M., 2019. Molecular Dynamics Simulation of Heat Transport through Solid-Liquid Interface during Argon Droplet Evaporation on Heated Substrates. Langmuir. https://doi.org/10.1021/acs.langmuir.8b04047.

Yu, X., Chiang, K.Y., Yu, C.C., Bonn, M., Nagata, Y., 2023. On the Fresnel factor correction of sum-frequency generation spectra of interfacial water. Journal of Chemical Physics 158. https://doi.org/10.1063/5.0133428.

Zeng, S.Y., Hsu, C.H., Wu, T.M., 2022. Bond Orientational Order Parameters for Classifying Solid-like Clusters in a Lennard-Jones System near Liquid-Solid Transition and at Solid States. Journal of Physical Chemistry A 126. https://doi.org/10.1021/acs.jpca.1c09527.

Zhan, C., Wang, G., Zhang, X.G., Li, Z.H., Wei, J.Y., Si, Y., Yang, Y., Hong, W., Tian, Z.Q., 2019. Single-Molecule Measurement of Adsorption Free Energy at the Solid– Liquid Interface. Angewandte Chemie - International Edition 58. https://doi.org/10.1002/anie.201907966.

Zhang, J., Song, H., Zhu, W., Wang, J., 2021. Liquid Transport Through Nanoscale Porous Media with Strong Wettability. Transp Porous Media 140. https://doi.org/10.1007/s11242-020-01519-5.

Zhang, L., Yang, H., Wang, G., Wang, Z., 2025. Molecular dynamics simulation on the heat transfer at liquid-solid interfaces and enhancement mechanism". Front Mech Eng 11. https://doi.org/10.3389/fmech.2025.1497939

Zhang, R., Zhang, X., Qing, S., Luo, Z., Liu, Y., 2023. Investigation of nanoparticles shape that influence the thermal conductivity and viscosity in argon-based nanofluids: A molecular dynamics simulation. Int J Heat Mass Transf 207. https://doi.org/10.1016/j.ijheatmasstransfer.2023.124031.

Zhang, X., Fujiwara, K., Shibahara, M., 2023. Interfacial thermal resistance calculations for weak solid–liquid atom interactions using equilibrium molecular dynamics. Mol Simul 49. https://doi.org/10.1080/08927022.2023.2202763.

Zhou, C., Li, J., Wang, S., Zhao, J., Ai, L., Chen, Qinggong, Chen, Qiya, Zhao, D., 2023. Development of Molecular Dynamics and Research Progress in the Study of Slag. Materials. https://doi.org/10.3390/ma16155373.

Zou, A., Poudel, S., Maroo, S.C., 2021. Confinement Effects on Molecular Mechanics and Structure of The Liquid Layers at Solid-Liquid Interface. ASME International Mechanical Engineering Congress and Exposition, Proceedings (IMECE). https://doi.org/10.1115/IMECE2021-70811.

Zêzere, B., Fonseca, T.V.B., Portugal, I., Simões, M.M.Q., Silva, C.M. and Gomes, J.R.B. 2023. Influence of Ethanol Parametrization on Diffusion Coefficients Using OPLS- AA Force Field. International Journal of Molecular Sciences, 24(8), article 7316. doi: 10.3390/ijms24087316.

APPENDICES

APPENDIX A
Solid plane for Butane

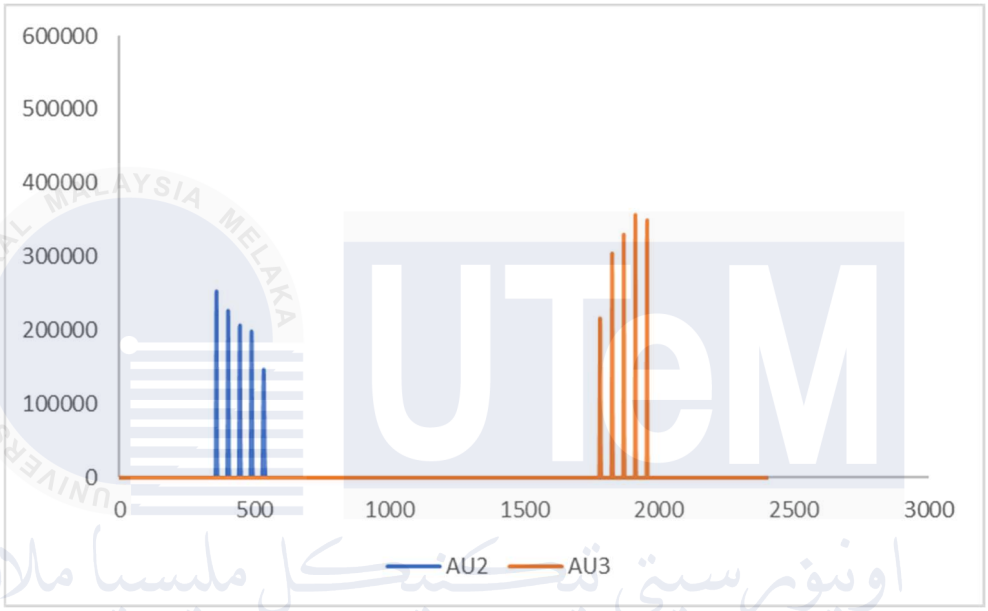

a) FCC 100

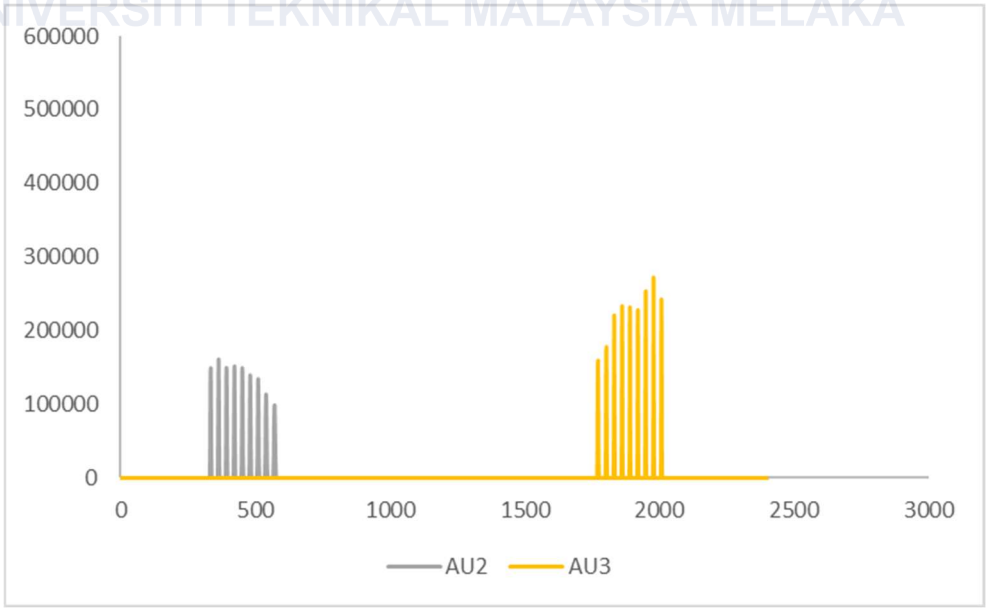

b) FCC 110

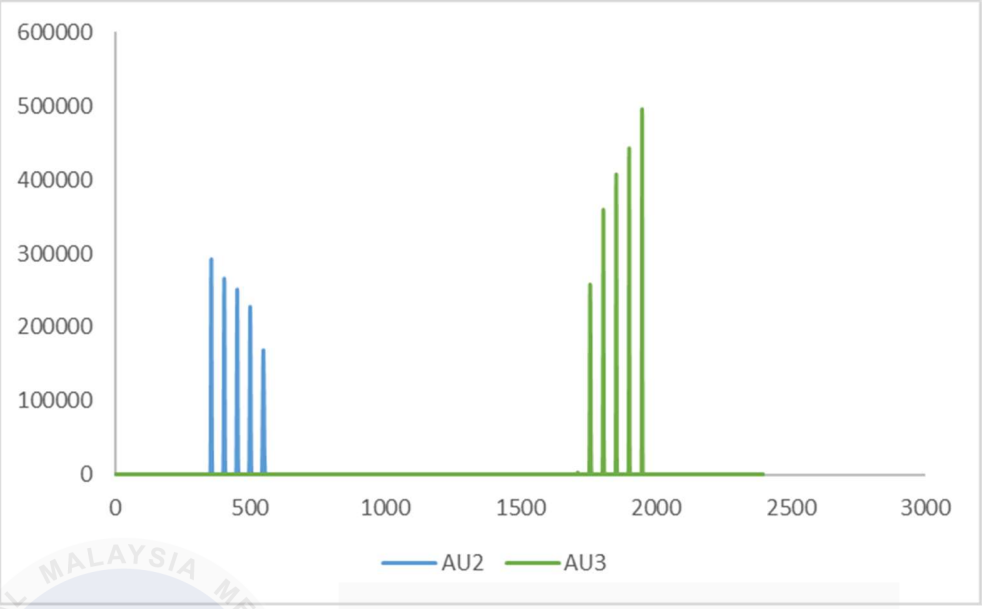

c) FCC 111

APPENDIX B
Solid plane for Pentane

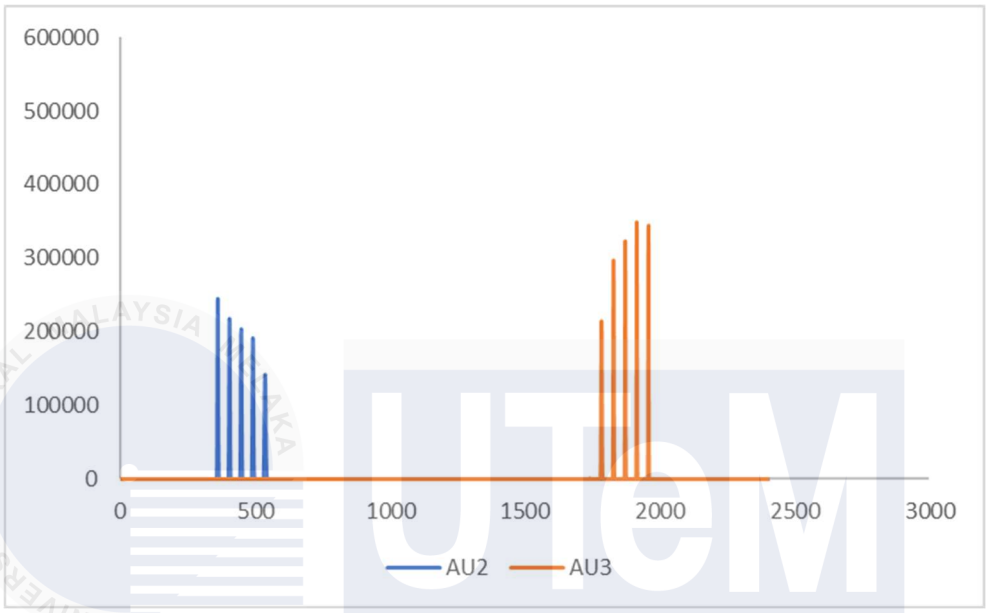

a) FCC 100

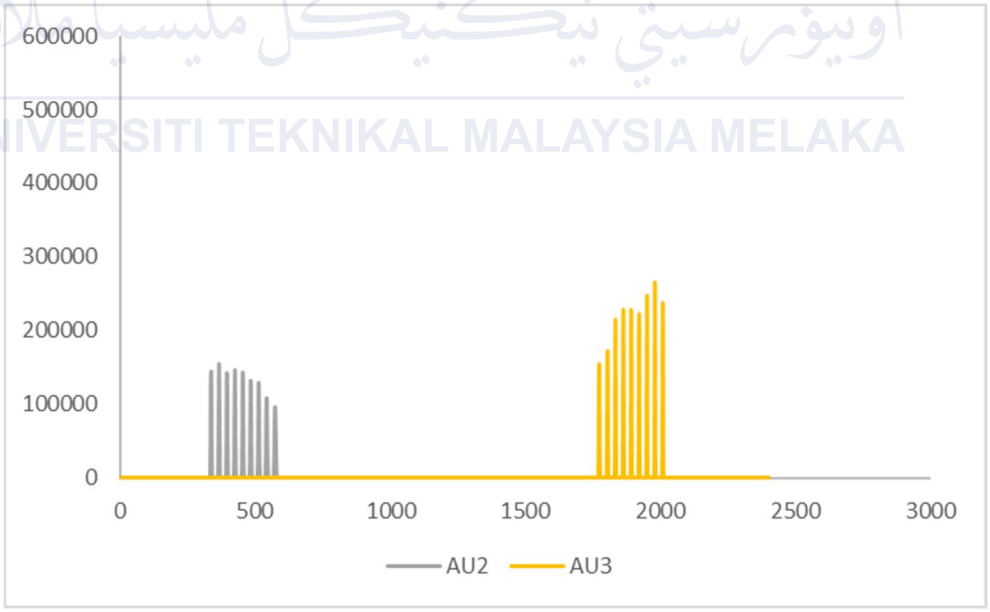

b) FCC 110

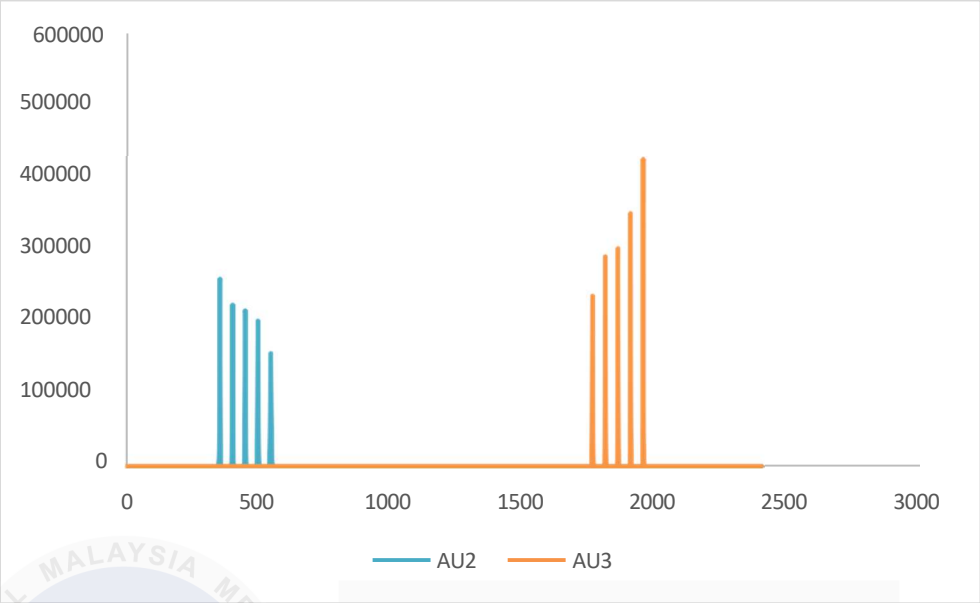

c) FC 111